Optimization of Susceptibility Weighted Imaging for Visualization of the 'Swallow Tail' in the Substantia Nigra

Joy Sng Xiao Wen

A0129673W

Supervisor: Dr. Mary Stephenson

Co-Supervisor: Dr. Chan Taw Kuei

Abstract

The purpose of this project is to improve the diagnosis of Parkinson's disease by optimising the susceptibility weighted imaging (SWI) sequence to visualise the 'swallow tail' sign in the substantia nigra.

To start off the project, MRI of the brain were done on young and healthy volunteers to obtain data that are necessary for the calculations and analysis in this project. With the data, brain maps were generated using MATLAB, and the T_1 and T_2^* values of our ROIs were measured. Following that, the SWI signal equation was derived and SWI simulations were conducted. Finally, the optimised parameters for our SWI sequence were determined to obtain the best contrasted SWI image of the swallow tail with maximum contrast-to-noise ratio.

The mean T_1 and T_2^* values of the swallow tail in the substantia nigra are found to be 1358 ± 325 ms and 20.7 ± 4.9 ms respectively, and the mean T_1 and T_2^* values of the tissues surrounding the swallow tail are 1303 ± 337 ms and 41.3 ± 7.2 ms respectively. The optimised parameters for the SWI sequence are found to be $\alpha = \cos^{-1}(\exp(-\frac{TR}{1255}))$, $TE = 27.8$ ms, and $TR \approx 60$ ms.

Acknowledgements

Table of Content

List of Figures

List of Tables

1 Introduction

This chapter gives readers an introduction to this project by explaining the key aspects, project rationales and scope of the project.

1.1 Background

Substantia nigra (SN) is part of the basal ganglia structure located in the anterior midbrain. Within the posterior third of SN, the largest cluster of dopamine containing neurons, known as the nigrosome-1, can be found. The nigrosome-1 shows up prominently on the iron-sensitive susceptibility weighted (SWI) magnetic resonance imaging (MRI) as it has a high SWI signal intensity while the surrounding SN – on its anterior, medial, and lateral sides – has an extremely low SWI signal intensity [1]. This results in the appearance of a split end of the 'swallow tail'. An illustration of these tissues can be seen in Figure 1.1 [1].
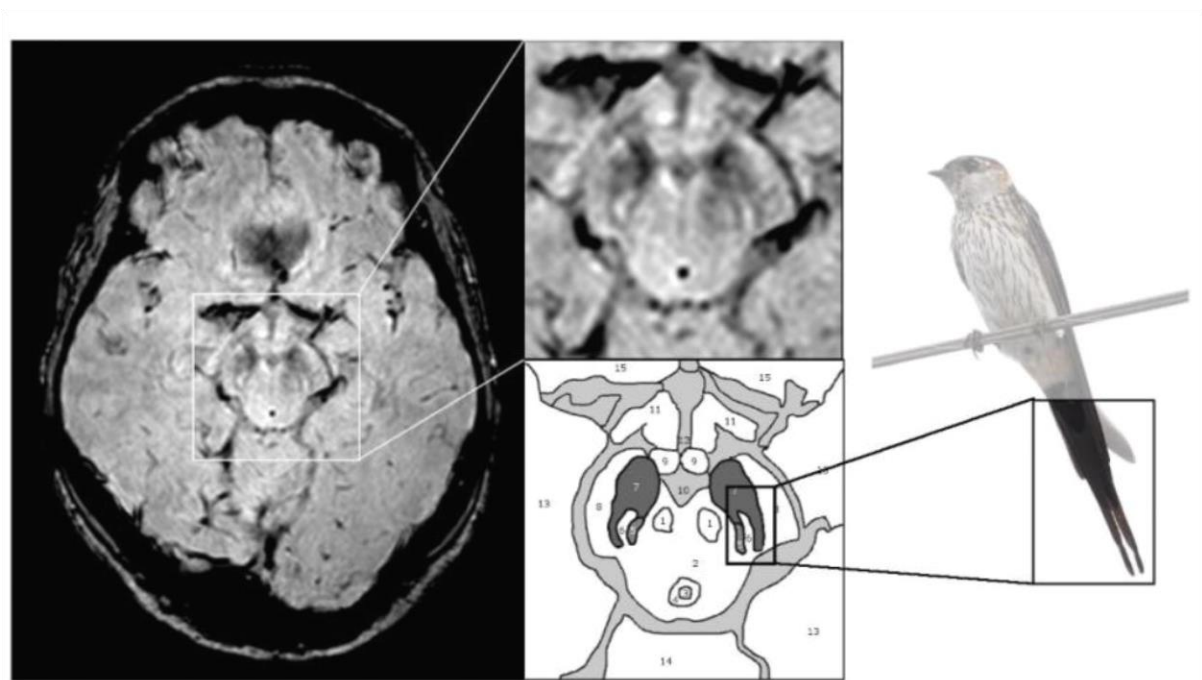
Figure 1.1: An axial slice of the brain showing substantia nigra. Nigrosome-1 is labelled '6', substantia nigra is labelled '7'. Comparison is made between the substantia nigra and the swallow tail. [1]

The low signal intensity of SN in SWI is attributed to its high iron content. In Parkinson's disease (PD) patients, there is an increase in iron deposit in the nigrosome-1, resulting in its loss of signal in SWI, and blending it with the adjacent SN [2]. At the same time, this 'swallow tail' sign will be lost. Although reasons for this occurrence are not fully understood yet, the latest reports stated that the nigrosome-1 can be affected by two ways in PD. One, there will be an increase in iron content, and two, there will be a decrease in neuromelanin content [2] [3] [4]. Neuromelanin stores iron and when it undergoes neurodegeneration, there will be a decrease in iron storage capacity which leads to more free iron in the region. Iron is known to have ferromagnetic properties which will affect the nuclear spins, leading to a loss of SWI signal. The region will be darkened, causing the 'swallow tail' sign to disappear. A comparison of the SN on a SWI image in a PD patient and a healthy person is shown in Figure 1.2 [4]. Notice that the nigrosome-1 has completely lost its SWI signal in the PD patient and hence, there is no visible 'swallow tail' sign.
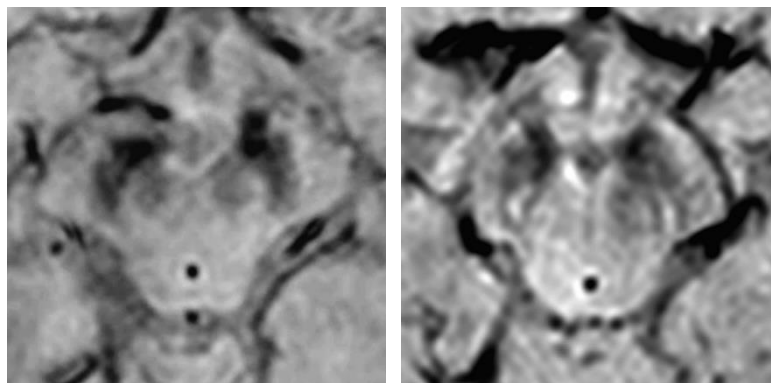
Figure 1.2: The substantia nigra in PD patient (left) and in a healthy person (right). [4]

Due to this interesting feature, high resolution SWI is used to visualise the 'swallow tail' sign in the substantia nigra for clinical diagnosis of PD [5].

1.2 Motivations

As mentioned in the previous section, SWI images of the SN are very useful in determining if a person has developed PD. However, it can be quite challenging to identify the swallow tail sign especially for SWI images with low signal contrast and resolution of the swallow tail. It has been reported that the diagnostic error rates are 4-15% in clinical trials and as high as 25% in community studies [5]. Proper diagnosis of PD is necessary as it prevents healthy people

from receiving unnecessary treatments and allows patients to receive the right treatment and medication earlier to better manage their symptoms and to delay the worsening of the disease.

Current clinical SWI protocols are not optimised for the diagnosis of PD. Hence, to solve the problem of misdiagnosis, we aim to find the optimised SWI sequence that will give us the best contrast and resolution of the swallow tail in the healthy population. With a better visualisation of the swallow tail, the diagnosis will hence be more accurate and reliable.

1.3   Project Objectives

In this project, the following steps were taken to obtain the best contrast and spatial resolution of the swallow tail in the SN:

1. Acquisition of MR images of the brain from young and healthy volunteers.
2. Generation of brain maps of various MRI constants (B_1, T_1 and T_2^*) using MATLAB.
3. Drawing of regions of interest (ROIs) using FSLView.
4. Calculation of MRI time constants of the ROIs.
5. Derivation of the MR signal equation in SWI.
6. Carrying out of SWI simulation on MATLAB.
7. Generation of signal contrast maps and determine parameters to optimise image.

The ROIs mentioned in step 3 consist of the swallow tail and its surrounding tissues. Ideally, the swallow tail should be as dark as possible (low signal intensity), and the surrounding tissues should be as bright as possible (high signal intensity).

The MRI time constants are unique in every tissue, and they dictate the change in signal intensities of the tissues during the imaging process. Thus, in step 4, we are essentially quantifying the ROIs with respect to their time constants before we proceed on to the rest of the analysis to find out how their signal intensities change over time during the SWI process. Since there may be uncertainties in the calculations of the time constants, we will be obtaining the values from a group of volunteers and calculate their mean values.

The equation derived in step 5 captures all the MR parameters and variables and gives us the magnitude of the signal intensity at any point of time during the imaging process. As it can quantify the signal intensities produced on SWI images, it is advantageous in helping us to visualise the tissue contrast.

In the SWI simulations in step 6, we will vary the parameters, observe the output signal contrast and signal contrast-to-noise ratio, and determine which parameters we should use to optimise the tissue contrast and resolution of the swallow tail and its surroundings. Signal contrast maps were generated in step 7 for better visualisation of the contrast in signal intensities, and from them, we can easily choose the parameters that give us the optimised SWI image.

2 Theory

This chapter covers the relevant physical concepts that are necessary for readers to have a better understanding of this project. The basic principles of the Magnetic Resonance Imaging (MRI) and Susceptibility Weighted Imaging (SWI) will be presented, followed by the calculations of the parameters that are essential in this project, such as the B_1, T_1 and T_2^* values. Note that B_1 is a property of the RF pulse and T_1 and T_2^* values are properties of the tissues.

2.1 Magnetic Resonance Imaging

MRI is an imaging technique that is used to obtain detailed images of organs, tissues, bones, and other internal structures of the human body for medical diagnosis purposes. Due to its ability to produce images with excellent soft tissues contrast and high spatial resolution, it is usually preferred over other imaging techniques, especially in cases where a high-resolution image is required for the detection of abnormalities is the soft tissues. MRI is non-invasive and it only uses strong magnetic fields and radiofrequency (RF) pulses which are safer than other methods that use ionising radiation which is a known cause of cancer and other irreversible chromosomal abnormalities [1] [6].

2.1.1 Interaction of Nuclear Spin with Magnetic Field

The operations of MRI are based on the principle of nuclear magnetic resonance (NMR), which is a physical phenomenon involving the interaction between a nucleus possessing a non-zero nuclear spin and an externally applied magnetic field $\overrightarrow{B_0}$ to create a net magnetisation.

A nuclear spin will be in a random position in the absence of magnetic field. When an external magnetic field is applied to the spin, it will immediately be influenced by the field, resulting in its precession about the direction of the field as illustrated in Figure 2.1 [7]. This direction is typically defined to be the direction of z-axis, also known as the longitudinal direction.
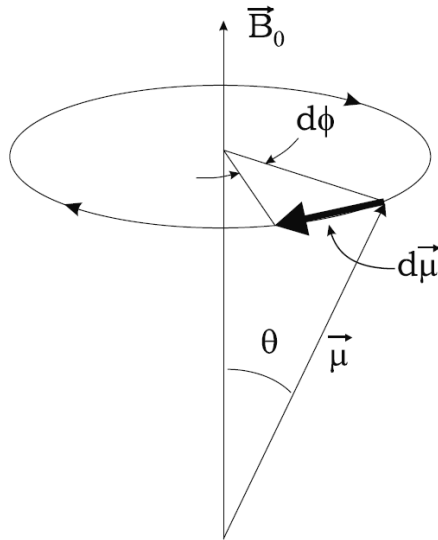
Figure 2.1: Precession of a nuclear spin $\vec{\mu}$ about the direction of the magnetic field $\overrightarrow{B_0}$.

The frequency of the spin's precession, also known as the Larmor frequency, is related to the magnetic field strength by:

$$\omega_0 = \gamma B_0 \tag{2.1}$$

where ω_0 is the Larmor frequency, γ is a gyromagnetic ratio unique to the nucleus, and B_0 is the applied magnetic field strength.

When a group of spins within a system is influenced by an externally applied magnetic field, there will be a collective distribution of precessing spins along the direction of B_0. This induces a net magnetisation within the system in the longitudinal direction. This system of precessing spins can be disturbed again when energy in the form of radiofrequency (RF) pulses at the Larmor frequency is applied. RF pulses will cause resonance to occur, and the spins will be deflected by an angle which is determined by the power of the RF pulse. This deflection angle is known as the flip angle. Due to this deflection, a net magnetisation in the xy-plane, known as the transverse magnetisation, will be resulted.

For a flip angle of 90°, the collective distribution of the precessing spins will rotate onto the transverse plane, resulting in a configuration where there is a maximum net transverse magnetisation and zero longitudinal magnetisation. This process is illustrated in Figure 2.2 [8].
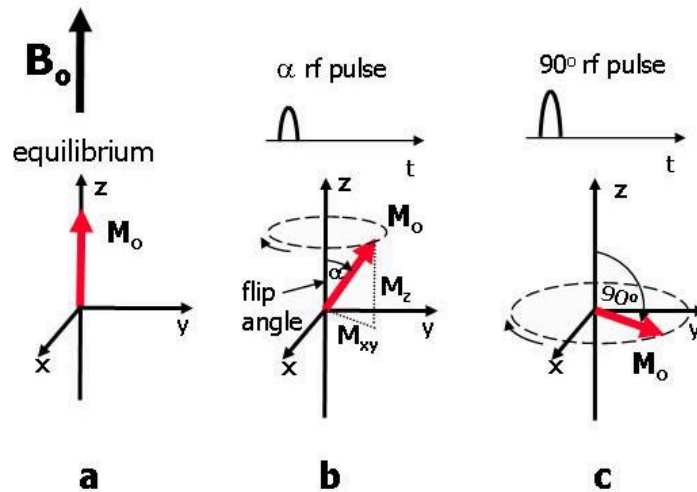
Figure 2.2: Interactions between precessing spins, external magnetic field, and RF pulse. (a) At equilibrium, the net magnetisation M_0 is in the longitudinal direction due to the precession of spins about the direction of the applied magnetic field B_0. (b) Upon the application of a RF pulse of flip-angle α, the magnetisation is deflected by α from the z-axis. The magnetisation now will be two components: longitudinal magnetisation M_z and transverse magnetisation M_{xy} (c) A RF pulse of 90° flip-angle will result in a maximum transverse magnetisation. [8]

Immediately after the RF pulse is applied, nuclear spins will start to lose energy and return to their equilibrium state, a process known as relaxation. During relaxation, the net longitudinal magnetisation increases back to its initial value before the application of the RF pulse at a rate given by T_1 (T_1 relaxation, see Sec. 2.1.2.1) while the net transverse magnetisation decreases back to zero at a rate given by T_2 or T_2^* (T_2 and T_2^* relaxation, see Sec. 2.1.2.2 and Sec. 2.1.2.3).

For imaging purposes in MRI, the external magnetic field is tuned to affect protons in the hydrogen nuclei. They are chosen due to their strong magnetic moment and high abundance in the human cells in the form of water and other organic molecules [9]. The body is subjected to a strong magnetic field and RF pulses when placed in the MRI scanner. Transverse magnetisation will generate a detectable signal which will be reflected in the MR images. Due to the different compositions in various biological tissues, their magnetic properties and relaxation rates differ, giving rise to contrasts in the images.

2.1.2 Relaxation Time Constants

Immediately after the application of RF pulse, spins start to lose energy and return to their equilibrium state. There are three types of relaxation upon the application of RF pulse. They are termed as T_1, T_2, and T_2^* relaxation.

2.1.2.1 T_1 relaxation

T_1 relaxation refers to the relaxation of the longitudinal magnetisation. It occurs because of the release of energy from the proton spin population during molecular motion. The rate of relaxation, and hence the change of the longitudinal magnetisation, is given by the Bloch equation:

$$\frac{dM_z}{dt} = -\frac{M_z - M_0}{T_1} \tag{2.2}$$

where $\frac{dM_z}{dt}$ is the rate of change of longitudinal magnetisation, M_z is the longitudinal magnetisation, M_0 is the equilibrium magnetisation, and T_1 is the longitudinal relaxation time constant or the time taken for approximately 63% of the original longitudinal magnetisation at equilibrium to be restored. This process is illustrated in Figure 2.3 [8].
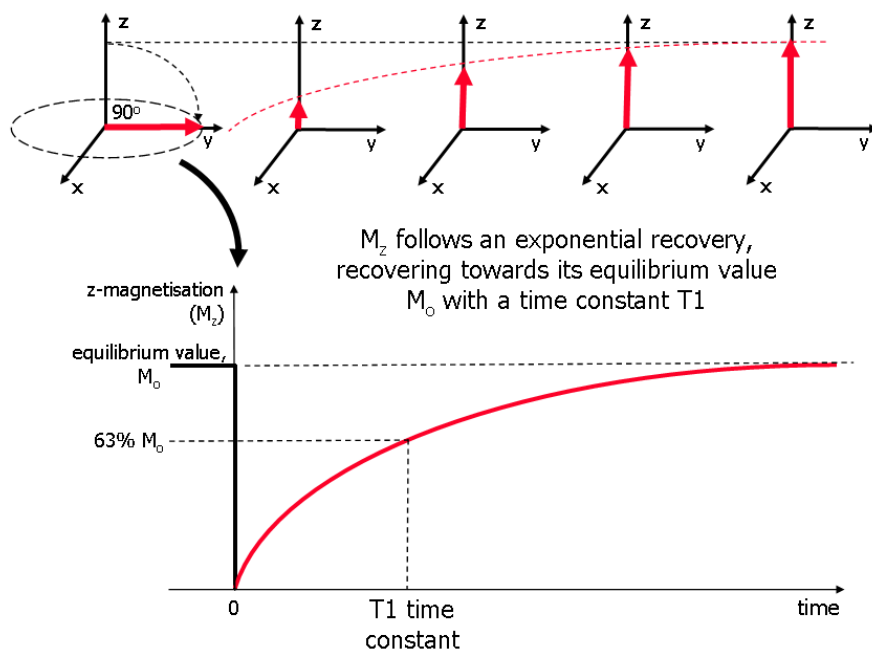
Figure 2.3: Process of T_1 relaxation after a 90° RF pulse is applied at equilibrium. The red arrows represent the direction and magnitude of the net longitudinal magnetisation. [8]

8

Upon solving equation (2.2), we arrive with the expression showing the evolution of the longitudinal magnetisation from the initial value $M_z(0)$ to the equilibrium value M_0 after a RF pulse is applied:

$$M_z(t) = M_z(0) \exp\left(-\frac{t}{T_1}\right) + M_0(1 - \exp(-\frac{t}{T_1})) \qquad (2.3)$$

2.1.2.2 T_2 relaxation

T_2 relaxation refers to the relaxation of the transverse magnetisation, and the rate of change is given by the Bloch equation:

$$\frac{dM_{xy}}{dt} = -\frac{M_{xy}}{T_2} \qquad (2.4)$$

where $\frac{dM_{xy}}{dt}$ is the rate of change of the transverse magnetisation, M_{xy} is the transverse magnetisation, and T_2 is the transverse relaxation time constant or the time taken for the transverse magnetisation to decrease to approximately 37% of its value just before relaxation.

Equation (2.4) yields the solution of the form:

$$M_{xy}(t) = M_{xy}(0) \exp(-\frac{t}{T_2}) \qquad (2.5)$$

showing the evolution of the transverse magnetisation from the initial value $M_{xy}(0)$ just after the RF pulse is applied.

Although T_1 (longitudinal) and T_2 (transverse) relaxation occur at the same time, T_2 relaxation usually occurs at a much faster rate. It should be noted that the net transverse magnetisation concerns the entire population of nuclear spins that are rotating in the transverse plane. In the beginning of the T_2 relaxation process, the spins will rotate together in a coherent fashion. They can be described as pointing in the same direction while rotating on the same transverse plane. At this stage, the spins are said to be rotating in phase. Over a period of time, they will eventually go out of phase, lose coherence and no longer rotate together. As they are now pointing in different directions, the summation of the transverse magnetisation will be further reduced. This is shown in Figure 2.4 [8].

In T_2 relaxation, the factor contributing to the dephasing effect is the spin-spin interactions. In a system of spins, it is possible for neighbouring spins to affect each other, slightly changing the magnetic field they are experiencing at a particular point of time even when the externally applied magnetic field remains constant. The Larmor frequencies of the spins deviate from one another, causing them to move out of phase. The dephasing of spins caused by spin-spin interactions is irreversible.

Another contributing factor of the dephasing effect that is reversible is the inhomogeneities in the external magnetic field. When the magnetic field is stronger or weaker, the Larmor frequency will be higher or lower, resulting in a decrease or increase in relative phase of the spins respectively. Inhomogeneities can be a result of imperfection of the MRI scanner or the difference in magnetic susceptibilities in the body tissues. This factor is not accounted for in the T_2 relaxation. Instead, it will be accounted for in the T_2^* relaxation which will be explained in the following section.

2.1.2.3 T_2^* relaxation

While T_2 encompasses the dephasing effect due to the interactions between neighbouring protons, T_2^* accounts for the additional dephasing of spins caused by the external field inhomogeneities. As such, T_2^* relaxation occurs at a much faster rate than T_2 relaxation. In this case, we will replace T_2 in equation (2.5) by T_2^*, which accounts for the more rapid decay of the transverse magnetisation.
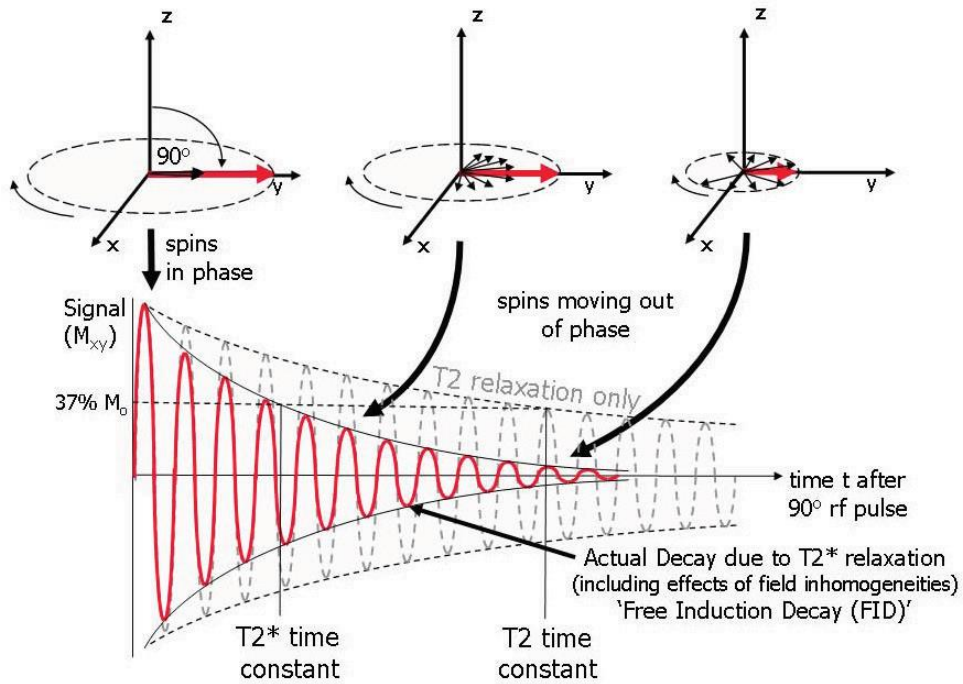
Figure 2.4: The process of transverse relaxation. The spins (small black arrows) rotate in phase initially and go out of phase eventually, causing a decrease in net magnetisation (red arrows). T_2 relaxation accounts for the dephasing effect due to spin-spin intereactions while T_2^* relaxation accounts for the dephasing effect due to spin-spin interations and magnetic field inhomogeneities.

The relationship between T_2 and T_2^* time constants is given by:

$$\frac{1}{T_2^*} = \frac{1}{T_2} + \frac{1}{T_2'} \tag{2.6}$$

where T_2' is the decay time that accounts for external field inhomogeneities. This additional decay caused by field inhomogeneities is constant with time and can be reversed by the application of a 180° refocusing pulse (see Sect. 2.1.3.1).

2.1.3 MR Image Acquisition

In this section, the two commonly used pulse sequences in MRI will be explained, they are the spin echo (SE) pulse sequence and the gradient echo (GRE) pulse sequence.

2.1.3.1 Spin Echo Pulse Sequence

SE pulse sequence gained its popularity when it is observed that field inhomogeneities had resulted in a rapid loss of signal [10]. To counter this effect, an echo is generated by applying a 180° refocusing RF after a 90° excitation RF pulse. An echo is characterised by a small peak in signal amplitude after the signal has decayed to zero. As such, the signal decay via the T_2 relaxation.

As mentioned previously, a 90° RF pulse will flip the magnetisation entirely onto the transverse plane and dephasing of the spins will occur overtime, causing signal to decay rapidly. The 180° refocusing RF pulse is applied after a certain time period, changing the positions of the spins. The faster spins will now be trailing behind the slower spins. Over a similar time period, the faster spins will catch up with the slower spins, moving back into phase and generate a peak in signal known as the spin echo. This refocusing RF pulse is said to have reversed the dephasing effect caused by magnetic field inhomogeneities. The SE pulse sequence is illustrated in Figure 2.5 [8].

For any pulse sequence, the **repetition time (TR)** is the time between consecutive points of a repeating series of excitation RF pulse and the **echo time (TE)** is the time between a RF pulse and the echo. Note that it is not necessary for the excitation RF pulse to be 90° and the SE pulse sequence will still work for any other flip-angles.
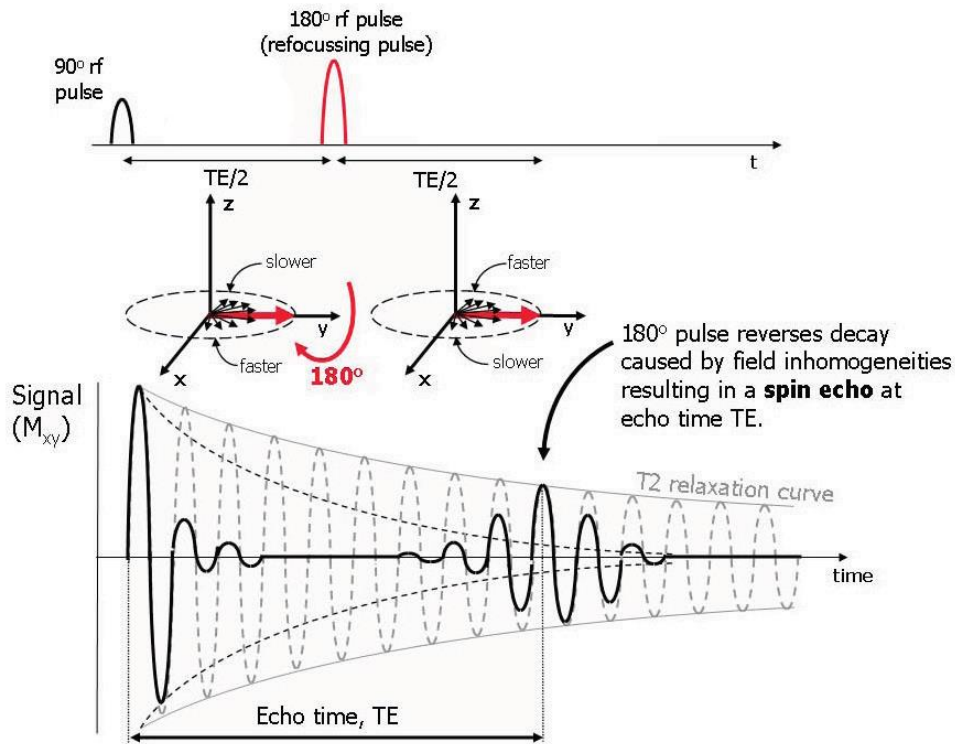
Figure 2.5: The process of a SE pulse sequence.

2.1.3.2 Gradient Echo Pulse Sequence

With the improvement of MR imaging systems which brought about better magnetic field uniformity, GRE sequence started gaining popularity over the years [10]. In contrast to the SE sequences, GRE sequences do not require a 180° refocusing pulse and thus, spins will retain the dephasing effect due to field inhomogeneities and the signal contrast is dictated by the T_2^* relaxation.

Within a MRI scanner, there consists of a cylindrical shell with conducting wire loops that are also known as "gradient coils". Current will be passed through the gradient coils to produce a secondary magnetic field known as the "magnetic field gradients" [11]. Since GRE sequences do no use refocusing RF pulses, echoes are generated through the measured application of magnetic field gradients, which are responsible for the alteration of the magnetic field strength in the system.

Initially, a positive magnetic field gradient is applied, increasing the rate of dephasing of the spins and signal decreases to zero rapidly. Next, a negative magnetic field gradient of the same

magnitude is applied to reverse the dephasing spins. This results in a gradient echo. After a period of time, the signal will decay back to zero again via the T_2^* relaxation curve. The GRE sequence is shown in Figure 2.6 [8].
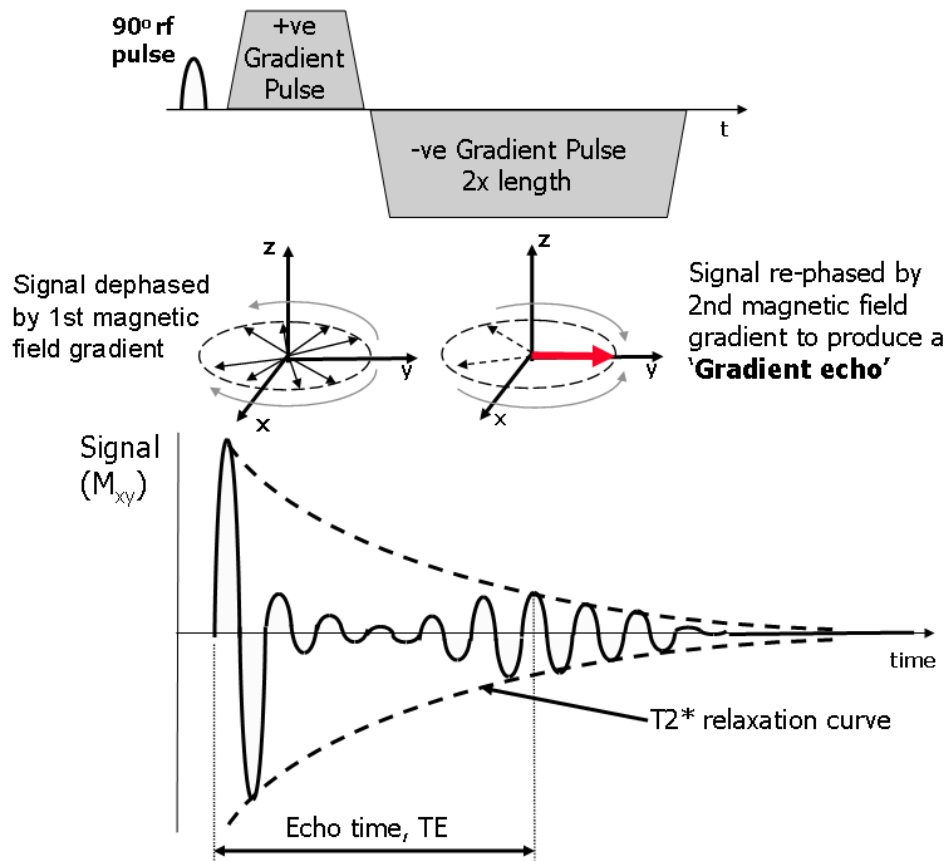
Figure 2.6: The process of a GRE pulse sequence. [8]

In GRE sequences, only spins that have been dephased by the first positive gradient pulse is refocused by the second negative gradient pulse. The dephasing effect resulting from field inhomogeneities are not compensated as they are in SE sequences.

Although GRE sequence is strongly affected by the presence of field inhomogeneities, this property can be put to an advantage. For instance, it can be used to detect the presence of iron when there is a haemorrhage in the brain as the image contrast is influenced by the magnetic susceptibility (see Sec. 2.2.1). In this project, this sequence will be useful in detecting iron in the SN. Another advantage of using the GRE sequence instead of SE sequence is the shorter acquisition time required due to the absence of the refocusing pulse in GRE.

2.2 Susceptibility Weighted Imaging

SWI is a neuroimaging technique to enhance contrast in MRI by exploiting the magnetic properties of tissues. Due to their magnetic susceptibilities (see Sec. 2.2.1), certain tissues can cause significant distortion of the external magnetic field, resulting in an additional dephasing of the spins. This effect is usually corrected in most diagnostic MRI sequences, which means that the resulting signals generated usually depend only on the magnitude information and do not reflect any information about the phase of the spins. However, phase images are important as they are able to give us information about the phase differences caused by the difference in tissue magnetic susceptibilities, which are useful in imaging tissues that are high in iron content or other compounds that will distort the field significantly [10].

SWI is a GRE sequence. It does not cancel the effect of field inhomogeneities, and hence, is able to create unique contrast between tissues by incorporating both the magnitude and phase information.

2.2.1 Magnetic Susceptibility

In SWI, the magnetic susceptibility of a tissue is of great importance because it determines the magnitude of magnetisation induced within the tissue when it is placed in an externally applied magnetic field. This will also induce a magnetic field in the tissue and distort the magnetic field outside the tissue. The higher the magnetic susceptibility, the greater the distortion of the field and the faster the spins move out of phase, resulting in a faster T_2^* relaxation.

The induced magnetisation of a material is given by:

$$\boldsymbol{M} = \chi \boldsymbol{B_0} \tag{2.7}$$

where $\boldsymbol{M}$ is the magnetisation induced in the material, χ is the magnetic susceptibility of the material, and $\boldsymbol{B_0}$ is the externally applied magnetic field.

From the magnetic susceptibility of a material, we can deduce the magnetic response of the material when it is placed in an externally applied magnetic field. These materials can be classified as paramagnetic, diamagnetic, and ferromagnetic.

Paramagnetic materials have a positive susceptibility ($\chi > 0$). They are weakly attracted by the external field and will induce magnetisation in the same direction as the field. They arise

when atoms contain unpaired electrons as they result in a non-zero spin or magnetic moments that will align with the external field and result in a net attraction. Examples of paramagnetic compounds that can be found in the human body are deoxyhaemoglobin, ferritin and hemosiderin [12].

In contrast to paramagnetic materials, diamagnetic materials have a negative susceptibility ($\chi < 0$) and they are repelled by the external field. They do not have unpaired electrons and have zero magnetic moments. In the presence of an external field, these materials will induce magnetisation that is opposite to the direction of the field according to Lenz's law. This kind of magnetisation can be found in bone minerals and calcification in the body tissue [12].

Ferromagnetic materials are strongly attracted by the external field and they retain magnetism after the removal of the field. They have positive susceptibility as in paramagnetic materials but is of several orders larger in magnitude. This kind of magnetism can be observed in tissues with high iron content, such as nigrosome-1 in Parkinson's disease patients [3].

The induced magnetic field is given by:

$$\boldsymbol{B} = \mu \boldsymbol{B_0} \tag{2.8}$$

where $\boldsymbol{B}$ is the magnetic field induced in the material, μ is the magnetic permeability of the material, and $\boldsymbol{B_0}$ is the externally applied magnetic field. The magnetic permeability can be written as: $\mu = \mu_0\mu_r$, where $\mu_o = 4\pi \times 10^{-7}$ is the permeability in vacuum and μ_r is the relative permeability of the material.

The magnetic susceptibility is related to permeability of the material as such:

$$\chi = \frac{\mu}{\mu_0} - 1 \tag{2.9}$$

From equations (2.7) to (2.9), the relationship between the induced magnetisation and the internally induced field can be expressed as:

$$\boldsymbol{M} = \frac{\chi}{\mu_0(1 + \chi)} \boldsymbol{B} \tag{2.10}$$

Since $\mu_0 \ll 1$, equation (2.10) shows that the induced magnetisation is directly proportional to the magnetic susceptibility of the material and the induced magnetic field. This explains why a material with higher magnetic susceptibility can cause a larger distortion to the magnetic field.

2.2.2 Phase Imaging

As mentioned previously, a SWI image can give better contrast compared to a typical MR image as it is formed by a combination of magnitude and phase images while the latter is only formed by the magnitude image.

The expression for phase is $\varphi = \omega_0 t$, making the change in phase between two tissues after a period of time TE to be:

$$\Delta\varphi = \Delta\omega_0 \text{TE} \tag{2.11}$$

where $\Delta\varphi$ is the change in phase, $\Delta\omega_0$ is the change in Larmor frequency, and TE is the echo time.

Substituting equation (2.1), equation (2.11) becomes:

$$\Delta\varphi = -\gamma\Delta B\text{TE} \tag{2.12}$$

where $\Delta B = B - B_0$. A phase image contains all information about the change in magnetic field, which can be classified as microscopic and macroscopic [10]. Microscopic refers to the change within the tissue caused by local iron deposit whereas macroscopic refers to the change caused by chemical shift, geometry of tissue, and inhomogeneities in the main field. As a result, equation (2.12) can be written as [10]:

$$\Delta\varphi = -\gamma\Delta(B_{local\ geometry} + B_{CS} + B_{global\ geometry} + B_{main\ field})\text{TE} \tag{2.13}$$

This last two terms are not within our interest and will be removed from the image by a high-pass filter. To obtain the finalised SWI image, we will multiply the filtered-phase image into the original magnitude image. Figure 2.7 shows the magnitude image, filtered-phase image, and a SWI image respectively that were obtained in this project.
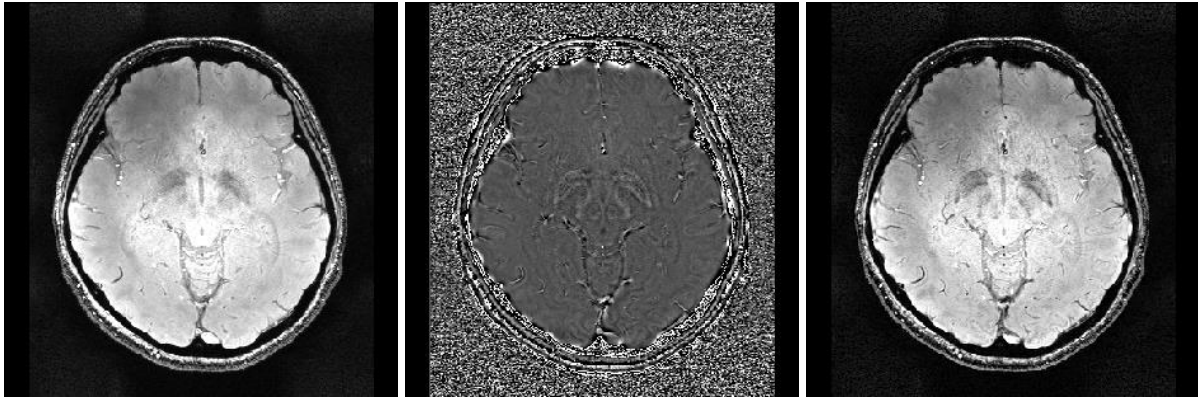
Figure 2.7: (left to right) Magnitude image, filtered-phase image, and SWI image.

Figure 2.8 shows the enlarged version of the magnitude and SWI images in Figure 2.7. Observe the distinct darker lines and regions in the grey matter of the SWI image due to the iron deposits.
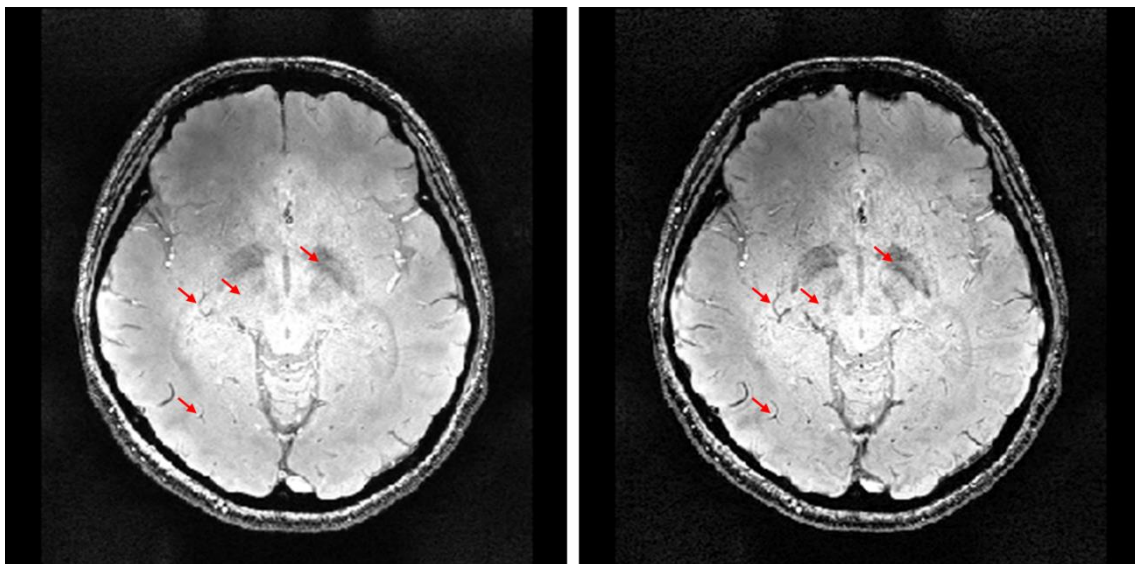
Figure 2.8: Enlarged version of magnitude and SWI image.

2.3   Measurement of Time Constants T_1 and T_2^*

An important step before performing our simulation in this project is to calculate the time constants, T_1 and T_2^*, of every voxel of the brain so that we can create a brain map and calculate the mean tissue parameters of the region we are interested in. T_2 calculation uses the same method as T2* calculation, however, it is not required in our project as SWI uses GRE sequence

where the longitudinal magnetisation decays via T_2^* relaxation. In this section, I will be discussing the theory and methodology for each measurement.

2.3.1 B_1 Calculation

Although B_1 is not a time constant, it is needed as part of the T_1 calculation by correcting the flip-angle. When RF pulse of a specific flip angle is applied during a MRI scan, the flip angles reflected across the MR image are usually not uniform. This effect is contributed by factors such as the RF pulse shape used, slice-selection gradients, resonance excitations, and magnetic field inhomogeneities [13]. To correct for this error in the flip angles, B_1 mapping of the entire brain was done to obtain the correction factor of the flip angle in each voxel of the image. It is important to obtain the actual flip angle as it will improve the accuracy of the T_1 calculations.

To obtain a B_1 map, data were acquired using the actual flip-angle imaging (AFI) pulse sequence [14]. In this pulse sequence, as illustrated in Figure 2.9, two identical RF pulses of the same flip angle α were applied, each followed by delays of different duration, TR_1 and TR_2 respectively. The signals S_1 and S_2 were obtained in the form of GRE.
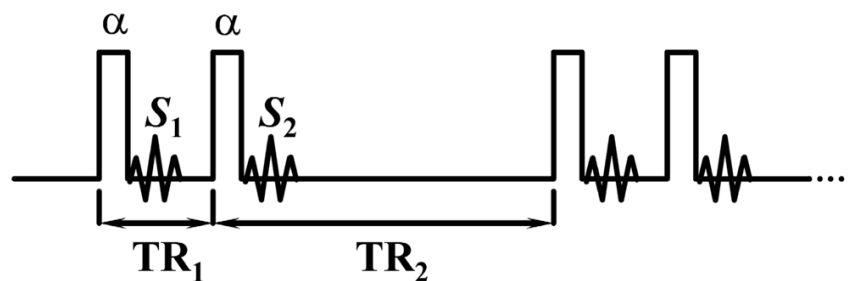
Figure 2.9: The actual flip-angle imaging (AFI) sequence [14].

There are two assumptions made in this pulse sequence. Firstly, relaxation effect of the magnetisation is significant, and the short TRs as compared to the T_1 timing has resulted in a pulsed steady state of magnetisation. Secondly, the sequence is assumed to be ideally spoiled. In other words, instead of waiting for the transverse magnetisation to decay completely, we deliberately cancel out the magnetisation by dephasing it with a spoiler gradient prior to the application of the next RF pulse. This is done to ensure that transverse magnetisation doesn't not interfere with the next RF pulse.

Based on the evolution of longitudinal magnetisation that we have established in equation (2.3), we can obtain the expressions for the longitudinal magnetisation after the nth and $(n + 1)$th excitation pulses respectively:

$$M_{z,n+1} = M_z(TR_1) = M_{z,n} \cos \alpha \, E_1 + M_0(1 - E_1) \tag{2.14}$$

$$M_{z,n+2} = M_z(TR_2)$$
$$= \left(M_{z,n} \cos \alpha \, E_1 + M_0(1 - E_1) \right) \cos \alpha \, E_2 + M_0(1 - E_2) \tag{2.15}$$

where $E_{1/2} = \exp\left(-\frac{TR_{1/2}}{T_1}\right)$. For a pulsed steady state condition, $M_{z,n} = M_{z,n+2}$. Solving them will give us the expressions for steady state longitudinal magnetisation:

$$M_{z,1} = M_z(TR_1) = \frac{M_0(1 - E_2 + (1 - E_1)E_2 \cos \alpha)}{1 - E_1 E_2 \cos^2 \alpha} \tag{2.16}$$

$$M_{z,2} = M_z(TR_2) = \frac{M_0(1 - E_1 + (1 - E_2)E_1 \cos \alpha)}{1 - E_1 E_2 \cos^2 \alpha} \tag{2.17}$$

Since the signals generated, S_1 and S_2, are related to the longitudinal magnetisation as such: $S_{1/2} = M_{z,1/2} \exp(-\frac{TE}{T_2^*}) \sin \alpha$, we can find the ratio of the signals by computing the ratio of the longitudinal magnetisation directly.

$$r = \frac{S_2}{S_1} = \frac{1 - E_1 + (1 - E_2)E_1 \cos \alpha}{1 - E_2 + (1 - E_1)E_2 \cos \alpha} \tag{2.18}$$

The short TR$_1$ and TR$_2$ in equation (2.18) allows us to expand the exponential terms using Taylor series up to the order of 1. As a result, the ratio of the signal magnitudes can be approximated to:

$$r \approx \frac{1 + n \cos \alpha}{n + \cos \alpha} \tag{2.19}$$

where $n = \frac{TR_2}{TR_1}$. Further manipulation of equation (2.19) will enable us to find the actual flip-angle:

$$\alpha_{actual} \approx \cos^{-1}\frac{rn - 1}{n - r} \tag{2.20}$$

Hence, by obtaining the signals of all the voxels across the images from this AFI sequence, we will be able to calculate the actual flip-angle of the spins in each of the voxel.

The B1 value is calculated by:

$$B_1 = \frac{\alpha_{actual}}{\alpha_{assumed}} \tag{2.21}$$

2.3.2 T$_1$ Calculation

T$_1$ values are calculated using the data obtained spoiled gradient recalled (SPGR) acquisition sequence [15]. SPGR sequence is similar to a typical GRE sequence with an additional establishment of a spoiled steady state. Using equations (2.3), we can derive the equation of the SPGR signal easily using the same method in the derivation of equation (3.3) (see Sec. 3.3). The resulting SPGR signal can be expressed as:

$$S_{SPGR} = \frac{M_0(1 - E_1)\sin\alpha}{1 - E_1\cos\alpha} \tag{2.22}$$

where S_{SPGR} is the signal obtained from the SPGR pulse sequence and $E_1 = \exp\left(-\frac{TR}{T_1}\right)$. Equation (2.22) can be represented in linear form as such:

$$\frac{S_{SPGR}}{\sin\alpha} = E_1\frac{S_{SPGR}}{\tan\alpha} + M_0(1 - E_1) \tag{2.23}$$

Multiple SPGR signal intensities can be obtained by varying flip-angle and keeping the other parameters constant. By plotting a linear best-fit graph of $\frac{S_{SPGR}}{\sin\alpha}$ against $\frac{S_{SPGR}}{\tan\alpha}$, we will be able to compute the T$_1$ values across all the voxels of the image by:

$$T_1 = \frac{-TR}{\ln(m)} \tag{2.24}$$

where m is the gradient of the graph.

2.3.3 T$_2$* Calculation

To calculate T$_2$*, data will be needed from the signals acquired using the GRE pulse sequence as described in section 2.1.3.2. The evolution of the transverse magnetisation will follow equation (2.5) except that the T$_2$ will now be replaced by T$_2$*. The equation can be expressed in a linear form as such:

$$\ln(M) = -\frac{TE}{T_2^*} + \ln(M_0) \tag{2.25}$$

By collecting multiple signal intensities with different TE while keeping other parameters constant, we can plot the best-fit graph of $\ln(M)$ against TE and compute the T$_2$* value by:

$$T_2^* = -\frac{1}{m} \tag{2.26}$$

where m is the gradient of the best-fit line.

3   Materials and Methods

This chapter presents the methods that were used in carrying out this project. The whole process will be divided into three parts – the collection of data through scanning of volunteers with a MRI scanner; construction of brain maps to determine the mean T_1 and T_2^* values of our regions of interest; and simulations of SWI using MATLAB to obtain the parameters that will give the optimised image. The optimised image is one that give us the best contrasted swallow tail with minimal background noise.

3.1   Collection of Data

In our study, all subject data were collected following signed informed consent for project approved by the National University Health System Domain Specific Review Board committee.

A pilot study was carried out initially by acquiring MR images using AFI, SPGR and GRE pulse sequences from two healthy and young volunteers. The MRI scanner used was the Siemens MAGNETOM Trio with a field strength of 3T.

After the first round of data analysis and confirming that the methods used are feasible, another round of acquisition was done to acquire more data with improved resolution. This time, 10 healthy volunteers between the ages of 22 and 26 were recruited for scans. The MRI scanner used for this round of study is the Siemens 3T MAGNETOM Prisma (Figure 3.1). This scanner is an upgraded model of the MAGNETON TRIO MRI scanner and has the potential to produce images with higher signal-to-noise ratio (SNR) and has a better field homogeneity [16].

Figure 3.1: Siemens 3T MAGNETOM Prisma.

The parameters used for the three imaging pulse sequences are as follow:

- **AFI Pulse Sequence (2 acquisitions)**

  TR = 50/150 ms

  TE = 4 ms

  Flip-angle = 60°

  Resolution: 64×64

  Pixel size: 3.4375×3.4375 mm^2

- **SPGR Pulse Sequence (4 acquisitions)**

  TR = 25 ms

  TE = 4.47 ms

  Flip-angle = 5/10/15/25°

  Resolution: 448×448

  Pixel size: 0.4911×0.4911 mm^2

- **GRE Pulse Sequence (10 acquisitions)**

  TR = 590 ms

  TE = 4.37/11.90/19.44/26.98/34.52/41.28/48.04/54.80/61.56/68.32 ms

  Flip-angle = 60°

  Resolution: 448×448

  Pixel size: 0.4911×0.4911 mm^2

As the human brain is a 3-dimensional structure, each acquisition consists of 16 slices of the brain, each with thickness of 2.0 mm. This means that the AFI images have voxel size of $3.4375 \times 3.4375 \times 2.0$ mm^3 while SPGR and GRE images have voxel size of $0.4911 \times 0.4911 \times 2.0$ mm^3. A single slice of the images collected using these three imaging sequences are presented in Figure 3.2.
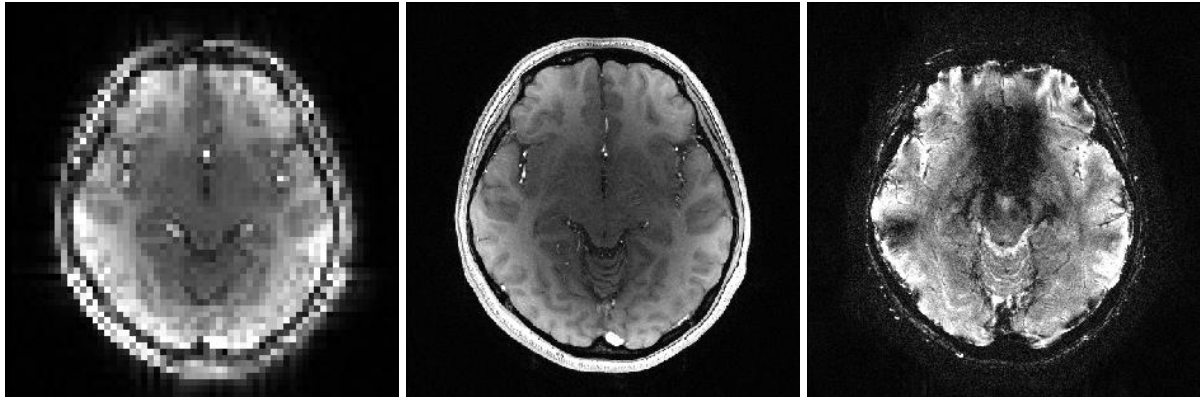
Figure 3.2: (From left to right) The 8th slice of AFI, SPGR, and GRE images.

3.2 Brain Mapping

Brain mapping is a process where quantities are being mapped onto the spatial domain of a brain image. In this project, the quantities that were mapped are the B_1, T_1 and T_2^* values, and this process was done using MATLAB. This section will provide explanations on how the brain mapping was done from the set of data of one volunteer.

3.2.1 Procedure

A total of three brain maps was generated for each volunteer. As a recap from section 2.3, B_1 maps are generated using data acquired from the AFI pulse sequence, T_1 maps are generated using data from the SPGR pulse sequence, and T_2^* maps are generated using data from the GRE pulse sequence.

For B_1 mapping, two AFI images were obtained. The signal intensities in every voxel of the two images were extracted and ratios of the values in corresponding voxels were calculated as in equation (2.19). The actual flip-angles and B_1 values in every voxel were calculated using equations (2.20) and (2.21) respectively. These B_1 values then formed the B_1 map of the brain as shown in Figure 3.3.
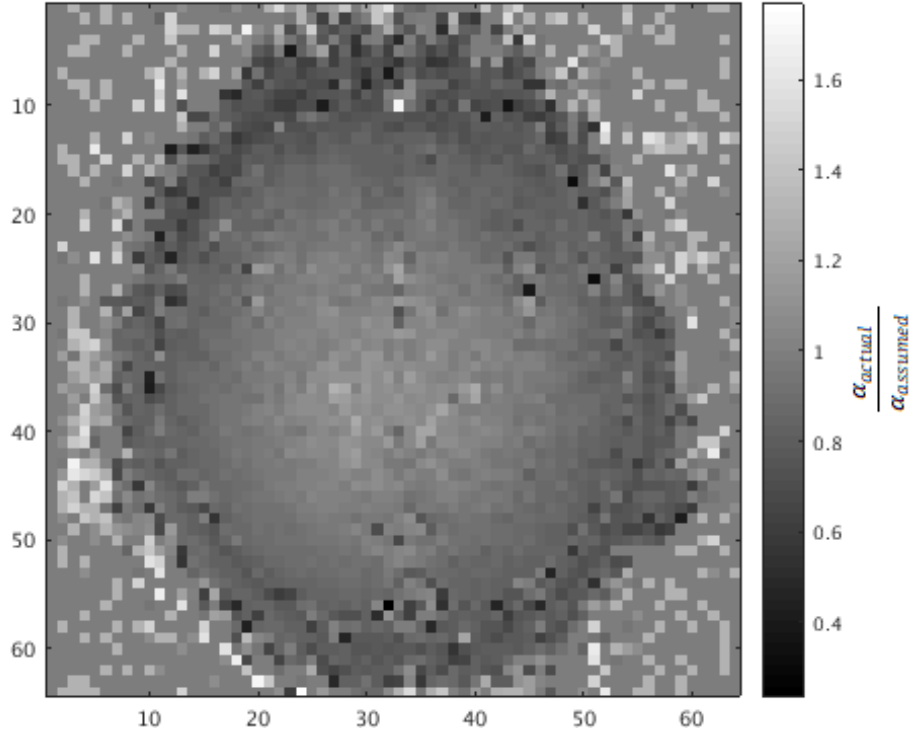
Figure 3.3: Slice 8 of B₁ map.

With the B_1 map, the actual flip-angle in every voxel of the SPGR images can be calculated simply by:

$$\alpha_{actual} = \alpha_{assumed} \times B_1 \tag{3.1}$$

The resolution of the SPGR images is 448×448 while the resolution of our B_1 map is only 64×64. Hence, on every slice of the B_1 map, each voxel was further split into 49 equal-sized voxels to ensure that they are of the same dimensions before proceeding to the T_1 mapping. The splitting of voxels was done by replicating each matrix element into 7 rows and 7 columns. The MATLAB code used is as follows:

```
for x = 1:64,
    for y = 1:64
        for z=1:16
b1imnew(7*x-6:7*x,7*y-6:7*y,z)=b1im(x,y,z);
        end
    end
end
```

where "b1im" is the original B_1 map and "b1imnew" is the modified B_1 map.

For T_1 mapping, four SPGR images were obtained with different flip-angles. Again, the signal intensities in each voxel of the images were extracted and fitted into a linear best fit line by performing polynomial curve fitting to the order of 1 on MATLAB. The T_1 values were calculated using equation (2.24) giving a T_1 map as shown in Figure 3.4.
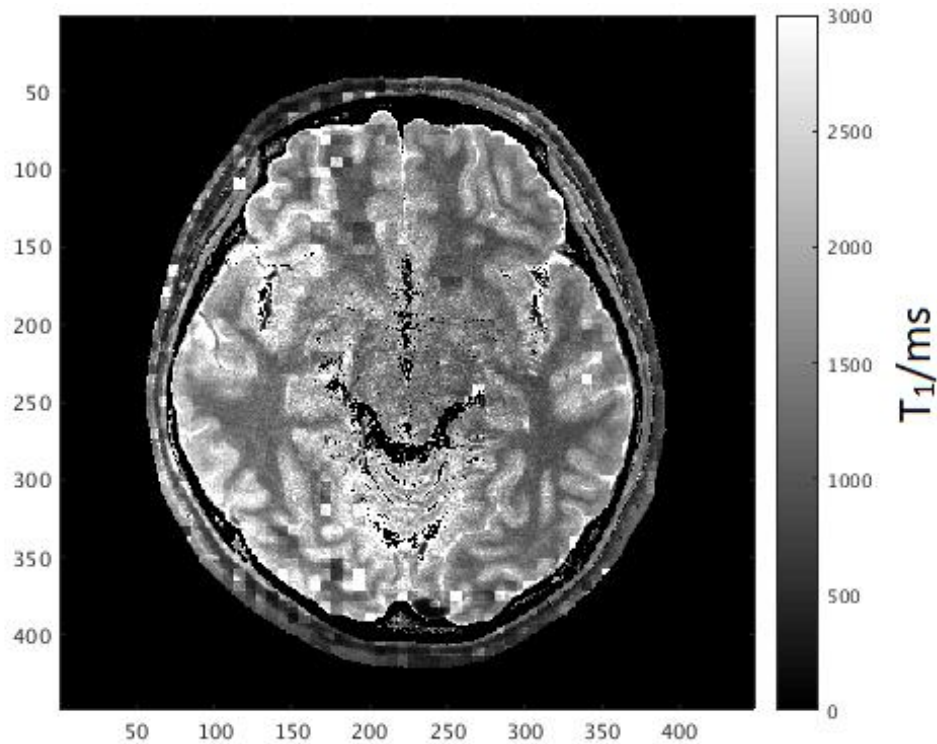
Figure 3.4: Slice 8 of T_1 map.

For T_2^* mapping, a similar process was done using 10 GRE images with different TE. The T_2^* values were calculated using equation (2.26) and a T_2^* map is formed as shown in Figure 3.5.
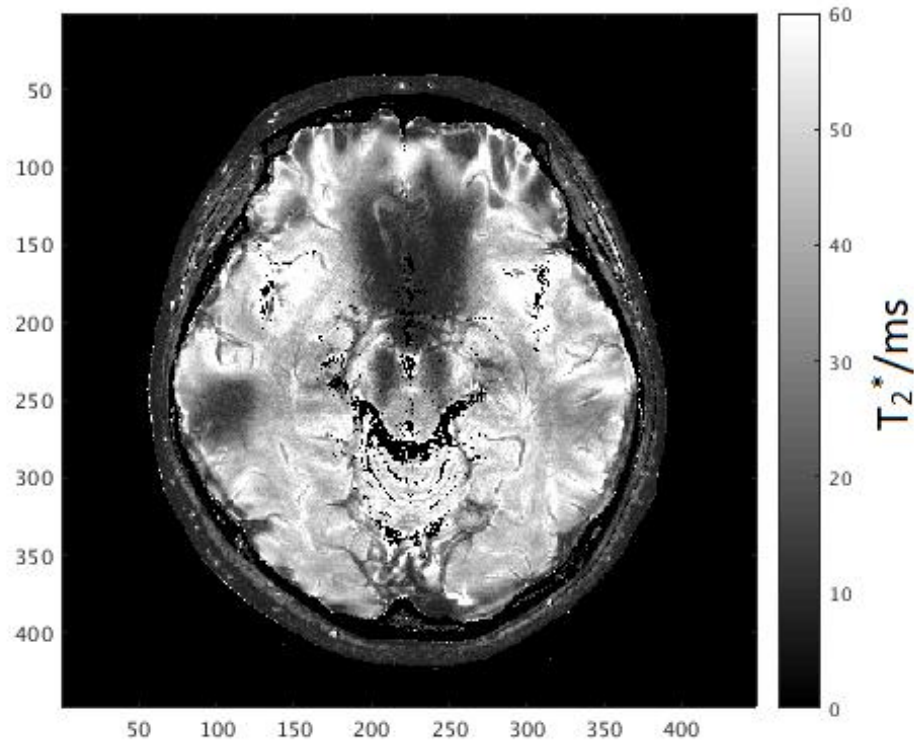
Figure 3.5: Slice 8 of T_2^* map.

3.2.2 Noise Elimination

The T_1 and T_2^* maps shown in Figures 3.4 and 3.5 above were obtained after noise elimination. Before noise elimination was done, the region outside the head was shown to have T_1 and T_2^* values. This is because signals were detected due to background noises.

The noise elimination was done by creating a brain mask and combining it with the original T_1 and T_2^* maps using MATLAB. Data from SPGR imaging were used to create the brain mask as they were found to have the best quality. The signals detected below threshold were suppressed completely while signals above the threshold were converted to 1. The threshold was chosen to be 50 as it was found to be the minimum value for the signal in the region outside the head to be completely suppressed. The resulting brain mask is shown in Figure 3.6.
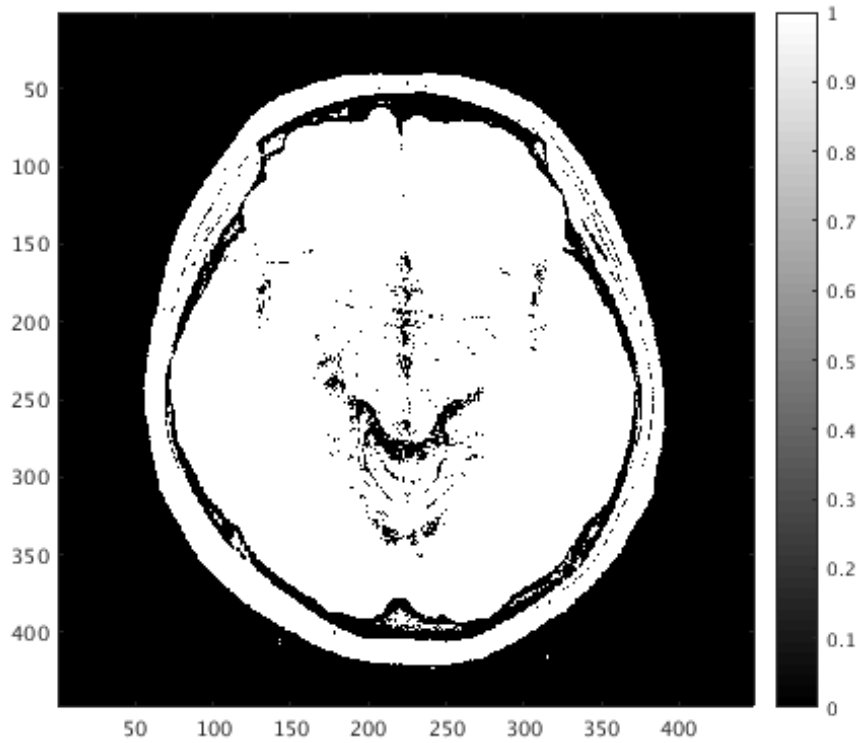
Figure 3.6: Slice 8 of brain mask.

Although the unwanted noises in the region outside the head will not affect the results of our project, this step is necessary for a better presentation of our T_1 and T_2^* maps.

3.2.3 Region Drawing

The ultimate purpose of creating the T_1 and T_2^* maps is to find the mean T_1 and T_2^* values of our regions of interest (ROIs). In this project, our aim is to maximise the contrast of the swallow tail and hence, the ROIs will be the area covered by the swallow tail (ST) and the area outside the swallow tail (OS).

In this part, we will be using a software FSLView [17] to create masks of our ROI. FSLView is designed for users to view the 3D image of the brain. It also allows users to create masks of the ROIs by selecting the essential voxels for every slice of the brain and converting their signals to 1 while leaving the unselected voxels as zero. A screenshot of the software is shown in Figure 3.7.

Figure 3.7: Screenshot of FSLView software.

Left: Orthographic view where one slice of coronal, sagittal, and axial planes are shown
simultaneously. Right: Single view showing one slice of the axial plane.

Figure 3.8 below shows an example of the selection of the voxels of our ROIs.
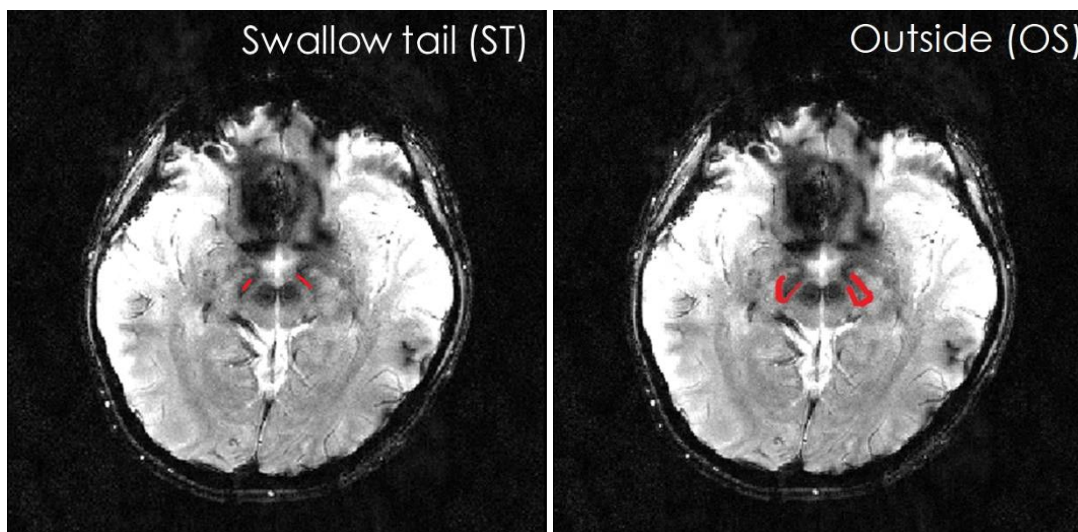
Figure 3.8: Selection of ROI using FSLView as shown by the red pixels.

Images from GRE sequence were used as they show a better image of the ST. With the ROI masks, we will combine them with our T_1 and T_2^* maps so that the T_1 and T_2^* values of our ROIs can be extracted out easily for the calculation of the mean values of these regions.

3.3 Derivation of SWI Equation

The SWI equation was derived before simulations were carried out. Figure 3.9 shows a complete cycle of a SWI pulse sequence. The first RF pulse of flip-angle α is applied at the beginning of the sequence. An echo is generated after a period of time TE, and the magnitude of the echo will be the detected signal for the generation of a MR image. After a period of time TR from the point of application of the first RF pulse of that cycle, another RF pulse of the same flip-angle α is applied and the cycle repeats.
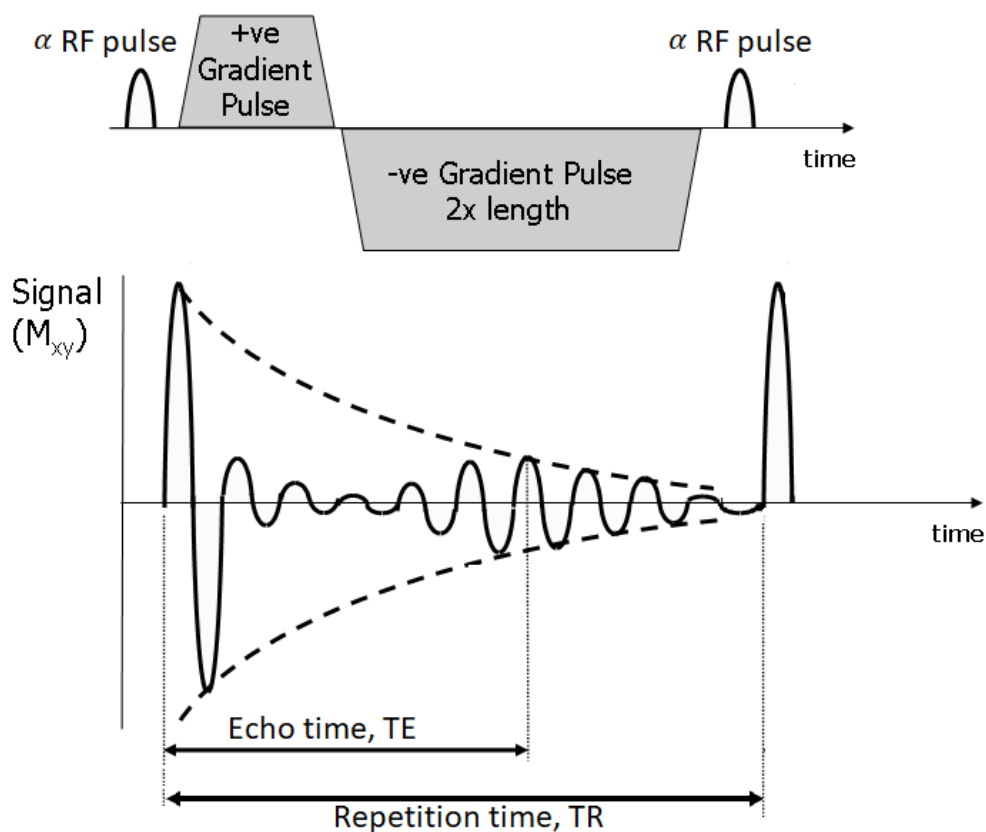
Figure 3.9: SWI pulse sequence.

In the following paragraphs, the steps taken for the derivation of the SWI signal expression are presented.

We started off with the expression for the evolution of the longitudinal magnetisation M_z as shown in equation (2.3). In practice, the SWI sequence is repeated multiple times and we will denote the magnitude of the longitudinal magnetism just before the application of the nth RF pulse be $M_{z,n}$. Note that when applying equation (2.3) in this context, $M_z(0)$ refers to the

longitudinal magnetisation just after the application of the RF pulse with flip angle α. Thus, $M_z(0) = M_{z,n} \cos \alpha$.

At the end the nth cycle, the magnetisation will be as given by the following expression:

$$M_{z,n+1} = M_{z,n} \cos \alpha \exp(-\frac{TR}{T_1}) + M_0(1 - \exp(-\frac{TR}{T_1})) \qquad (3.2)$$

We further assume that the SWI sequence satisfies the condition $M_{z,n} = M_{z,n+1}$, which is also known as the pulse steady-state condition. Putting in words, a pulsed steady state is satisfied when the longitudinal magnetisation just before each application of a RF pulse is of a constant value.

Solving this equation will give us the longitudinal magnetisation in the following steady state:

$$M_{z,n} = \frac{M_0(1 - \exp(-\frac{TR}{T_1}))}{1 - \exp\left(-\frac{TR}{T_1}\right) \times \cos \alpha} \qquad (3.3)$$

Finally, the magnitude of the echo after time TE and hence the signal expression for SWI images can be expressed as:

$$M_{xy} = \frac{M_0(1 - \exp(-\frac{TR}{T_1})) \times \sin \alpha \times \exp(-\frac{TE}{T_2^*})}{1 - \exp(-\frac{TR}{T_1}) \times \cos \alpha} \qquad (3.4)$$

where M_{xy} is also the magnitude of the signal shown on the SWI images.

3.4 Simulations

Lastly, we proceeded to the simulations of SWI. The SWI sequence is as shown in Figure 3.9. Using MATLAB, equation (3.4) and the measured mean T_1 and T_2^* of the ROIs were used to calculate the signals generated in the respective ROIs of the simulated SWI images (S_{OS} and S_{ST}). Results were then used to produce signal contrast maps. These maps serve to

help us observe how we can modify our parameters (flip-angle, TE, and TR) to obtain the most optimised SWI image. We determine whether an image is optimised by studying the signal contrast and the contrast-to-noise ratio (CNR).

All possible combinations of the parameters were chosen to perform our simulations to optimise the signal contrast and CNR between OS and ST. There were three sets of simulations:

1. Fixed parameter: TE (30/50/100/200 ms)
   Varied parameters: TR (0 – 200 ms), flip-angle (0 – 90 deg)
2. Fixed parameter: flip-angle (optimised)
   Varied parameters: TR (0 – 200 ms), TE (0 – 100 ms)
3. Fixed parameters: TE and flip-angle (both optimised)
   Varied parameter: TR (0 – 5000 ms)

To create a better visualisation of the ST, we must increase the contrast between the ST and OS. The signal contrast is defined as:

$$Signal\ Contrast = S_{OS} - S_{ST} \qquad (3.5)$$

where S_{OS} is the signal for the brighter OS region and S_{ST} for the darker ST region.

In addition to increasing the signal contrast, it is also important to increase the CNR. SWI images are formed by a combination of signals and unwanted background noise which will decrease the quality of the image. This noise is mainly a result of the random molecular movement and electrical resistance [18]. Although background noise is unavoidable, we can reduce its effect by increasing the CNR.

There are many ways to increase and CNR, and in this study, we will do so by acquiring the same signals repeatedly to form the same image. The number of signals acquired is termed as the "number of averages" [18].

The formula of CNR is given as such:

$$CNR = \frac{S_{OS} - S_{ST}}{\sigma} \times \sqrt{n} \qquad (3.6)$$

where n is the number of averages, and σ is the signal intensity of the background noise. Since σ is a constant, we can substitute it with any arbitrary value.

The number of averages (n) is determined by the total scan time and TR as such:

$$n = \frac{total\ scan\ time}{TR}$$

<div align="right">(3.7)</div>

Hence, if we were to keep to a specific scan time, we will be able to acquire more signals with a shorter TR. This will in turn improve the CNR of the image.

4 Results and Discussions

This chapter contains the results obtained after the analysis of all the MRI data as well as the discussions of the results.

4.1 Time Constants

From the data collected from the 10 healthy volunteers between the ages of 22 and 26, we have removed some of them which were found to be flawed. For the remaining data, the T_1 and T_2^* of the regions of interest (ROIs) were measured and presented in Table 1. The mean T_1 and T_2^* values, together with their standard deviations, are presented in Table 2. The ROIs on the T_1 and T_2^* maps are shown in Figure 4.1.

Volunteer	ROI	T_1 (ms)	T_2^* (ms)
1	OS	1239	47.7
	ST	1300	24.7
2	OS	1306	47.1
	ST	1382	23.1
3	OS	1224	54.9
	ST	1389	26.2
4	OS	1231	42.6
	ST	1449	21.8
5	OS	1351	49.5
	ST	1245	20.2
6	OS	1274	45.8
	ST	1549	16.7
7	OS	1378	35.9
	ST	1321	17.9
8	OS	1424	39.7
	ST	1230	17.5

Table 1: Individual T_1 and T_2^* values of the ROIs, OS refers to outside swallow tail and ST refers to swallow tail.

ROIs	$T_1 \pm SD$ (ms)	$T_2^* \pm SD$ (ms)
Outside ST (OS)	1303 ± 337	41.3 ± 7.2
Swallow Tail (ST)	1358 ± 325	20.7 ± 4.9

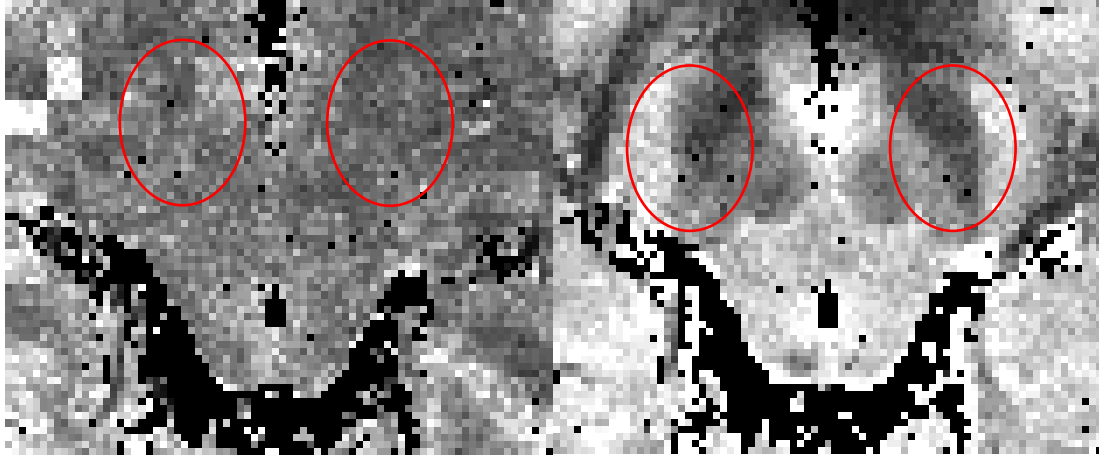*Table 2: Mean T_1 and T_2^* values of the ROIs*

Figure 4.1: T_1 (left) and T_2^* (right) maps of the same slice zoomed in to the region containing the ROIs in red circles.

The T_1 values of ST and OS are approximately equal, showing that the rate of longitudinal relaxation of the spins in both regions is about the same. This is also reflected in Figure 4.1 as the ST and OS are not distinguishable on the T_1 map.

A significant difference in the T_2^* value between ST and OS is observed across all the volunteers. The mean T_2^* value, as shown in Table 2, is found to be 2 times smaller in ST than in OS. This observation reaffirms us about the presence of iron in the ST, which has a higher magnetic susceptibility that causes larger distortion in the magnetic field, resulting in a faster signal decay rate as compared to the OS which does not contain iron. In Figure 4.2, we can see that the ST and OS are distinguishable on the T_2^* map.

4.2 Optimised SWI Parameters

There are three parameters that we have optimised in the SWI sequence. They are the flip-angle (FA), TE, and TR. Using the mean T_1 and T_2^* values that we have calculated in the previous

section, we performed SWI simulations on MATLAB and the results obtained are presented in the next three subsections.

4.2.1 Optimisation of Flip-Angle

We started with the optimisation of FA. Simulations for a range of TRs (0 – 100 ms) and FAs (0° – 90°) were conducted while keeping TE fixed. From the results, we have generated signal contrast map of TR against FA. As we do not know the optimal TE, this procedure was repeated with different TEs. This is also done to study how changing TEs will affect our results. The TEs chosen were 30, 50, 100, and 200 ms. The contrast maps are shown in Figure 4.2. In these contrast maps, yellow represents high contrast of the ST while blue represents low contrast.
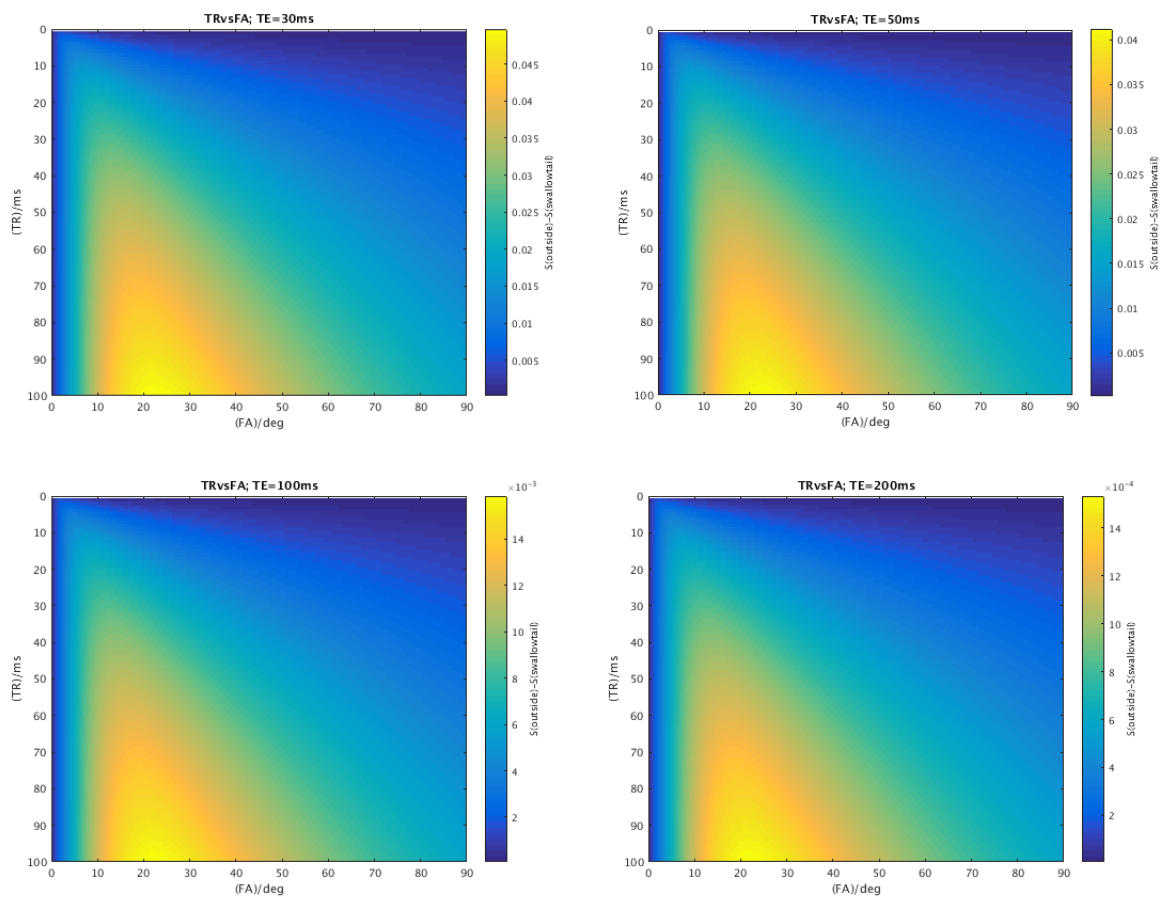

Figure 4.2: Signal contrast maps of TR against FA at various TEs (30/50/100/200 ms).

From each of these contrast maps, the values of the signal contrasts were extracted and plotted out against the FA for different TRs (30/40/50/60 ms). This is to help us visualise the results. The corresponding graphs are as shown in Figure 4.3.
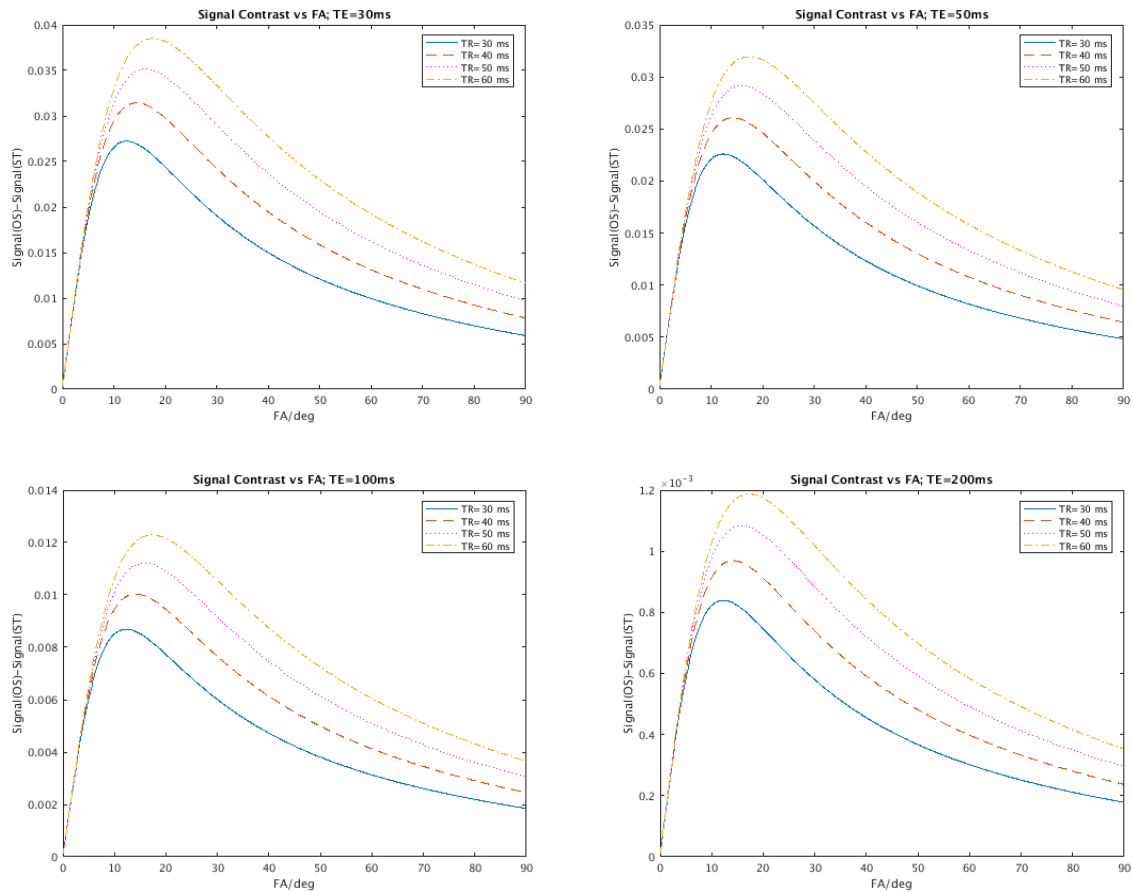
Figure 4.3: Graphs of Signal Contrast against FA for different TRs (30/40/50/60 ms) at different TEs (30/50/100/200 ms).

The peaks of the graph tell us the FA that will give us the best signal contrast of ST and OS. This angle is known as the optimal FA. Here are the deductions we have drawn from the graphs in Figure 4.3:

1. Signal contrast increases with TR. This is evidenced by the increasing height of the peak when TR increases.
2. Optimal FA is independent of TE. This is evidenced by the signal contrast peaks staying relatively at the same positions on the FA-axis for different TEs.
3. Optimal FA increases with increasing TR. This is evidenced by the signal contrast peaks shifting to the right as the TR increases from 30 ms to 60 ms.

Attempts were made to estimate the relationship between optimal FA and TR. It was found that the relationship between them are the same as how the angle and TR are related in the Ernst angle (α_E) formula as given by:

$$\alpha_E = \cos^{-1}(\exp(-\frac{TR}{T_1}))$$ (4.1)

Ernst angle is the angle that gives the greatest signal intensity of one tissue for a given TR and it may not give the best signal contrast between two different tissues [19]. However, it is observed in our case that the signal contrast is the closest to its optimum when T_1 of OS is used.

The Ernst angles for OS and ST at the different TRs are presented in Table 3, and the optimal FAs found from each of the graphs at different TRs and their percentage discrepancies with respect to the Ernst angle for OS are presented in Table 4.

TR/ms	Ernst Angle for OS (deg)	Ernst Angle for ST (deg)
10	7.1	6.9
20	10.0	9.8
30	12.2	12.0
40	14.1	13.8
50	15.8	15.5
60	17.3	16.9
70	18.6	18.2
80	19.9	19.5
90	21.0	20.6
100	22.2	21.7

Table 3: List of Ernst angles with their corresponding TRs.

TR/ms	TE30		TE50		TE100		TE200	
	Actual (deg)	%descrep.	Actual (deg)	%descrep.	Actual (deg)	%descrep.	Actual (deg)	%descrep.
10	7.2	-1.57	7.2	-1.57	7.1	-0.16	7.1	-0.16
20	10.2	-1.88	10.1	-0.88	10.0	0.12	10.0	0.12
30	12.5	-2.07	12.4	-1.26	12.3	-0.44	12.2	0.38
40	14.4	-1.97	14.2	-0.55	14.2	-0.55	14.1	0.16
50	16.1	-2.10	15.9	-0.83	15.8	-0.20	15.8	-0.20
60	17.6	-2.02	17.4	-0.86	17.3	-0.28	17.3	-0.28
70	19.0	-2.09	18.8	-1.02	18.6	0.06	18.6	0.06
80	20.2	-1.66	20.0	-0.65	19.9	-0.15	19.9	-0.15
90	21.4	-1.67	21.2	-0.72	21.1	-0.25	21.1	-0.25
100	22.6	-1.99	22.3	-0.64	22.2	-0.19	22.2	-0.19

Table 4: Optimal FAs at their corresponding TRs for different TE (30/50/80/200 ms). The percentage discrepancies are calculated with respect to the Ernst angle for OS.

The low percentage discrepancies between the actual optimal FA and the Ernst angle for OS show that we can use the Ernst angle formula as an approximation for the optimal FA. It is also found that as TE increases, the actual optimal FA will increase and tend towards the Ernst angle for OS. Note that this optimal FA can be fine-tuned and approximated more accurately by changing the constant "T_1" in equation (4.1) after the optimal TE is known.

4.2.2 Optimisation of TE

After determining the optimal FA, we proceeded to the optimisation of TE. In this part, we have conducted simulations for a range of TRs (0 – 200 ms) and TEs (0 – 100 ms). The FA is optimised according to the Ernst angle formula in equation (4.1). The signal contrast map of TR against TE is shown in Figure 4.4. In this contrast map, yellow represents high contrast of the ST while blue represents low contrast. We have also plotted the signal contrast against TE as shown in Figure 4.5.
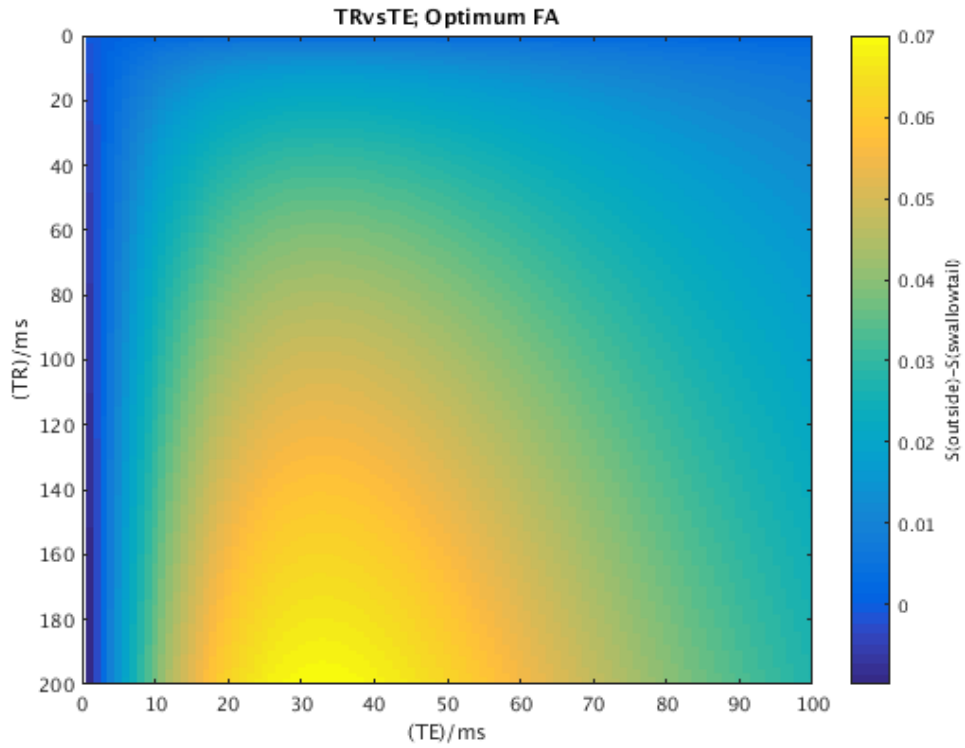
Figure 4.4: Signal contrast maps of TR against TE, using Ernst angle as the optimal FA
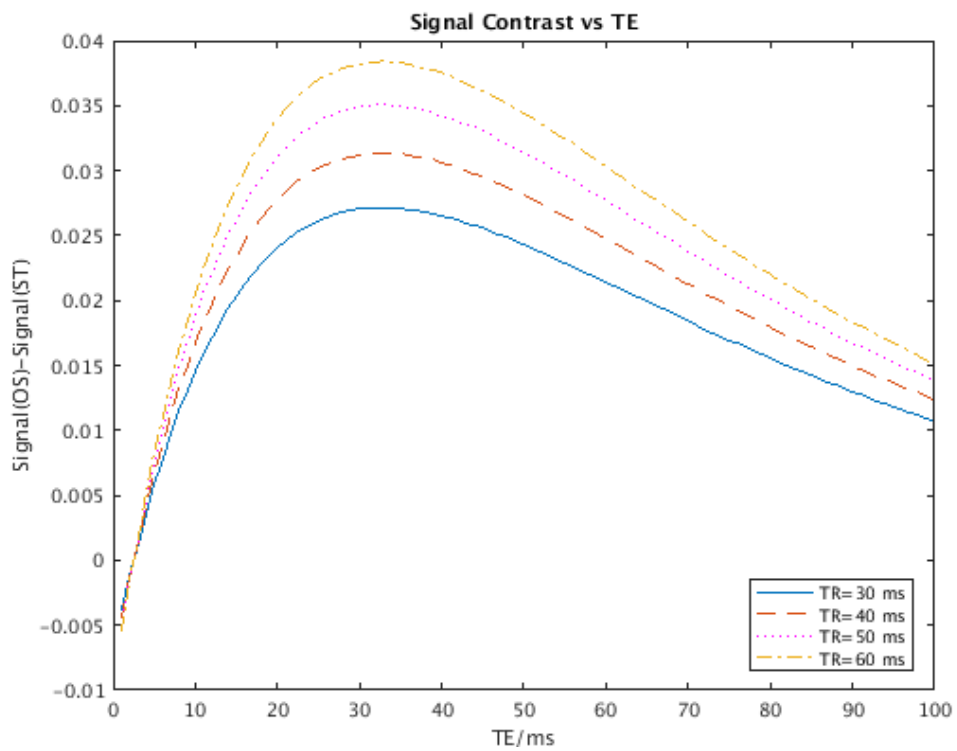

Figure 4.5: Graph of Signal Contrast against TE for different TRs (30/40/50/60 ms).

As the peak shows the TE that gives us the best contrast of the ST, we can conclude from Figure 4.5 that the optimal TE is independent of TR. From the graph, we can also clearly see that with longer TR, the intensity of the signal contrast increases.

For "`S`" representing the matrix of the signal contrast map as shown in Figure 4.4, the function "`I= max(S(:))`" was used on MATLAB, where the value of the largest signal contrast is determined. Next, the function "`[I_row,I_col]=ind2sub(size(S),I)`" was used to determine which row (`I_row`) and column (`I_col`) contain this maximum signal contrast respectively. "`I_col`" reflects the optimal TE and it was found to be the consistent across every row, again proving that optimal TE is independent of TR.

In this study conducted on the young and healthy volunteers, the optimal TE is found to be 27.8 ms. Since the optimal TE is closer to 30 ms, the optimal FA will be approximated by:

$$\alpha_{optimal} = \cos^{-1}(\exp(-\frac{TR}{1255})) \qquad (4.2)$$

This gives us the angle that is closest to the actual optimal FA for TE of 30 ms as shown in Table 4.

4.2.3 Optimisation of TR

Finally, after obtaining the optimised FA and TE, we investigated the optimal TR. The optimised FA and TE were used in this simulation. From the results, a graph of signal against TR is plotted as shown in Figure 4.5. Three signal graphs were plotted, and they are the individual signal of OS and ST, and the signal contrast ($S_{OS} - S_{ST}$) respectively.
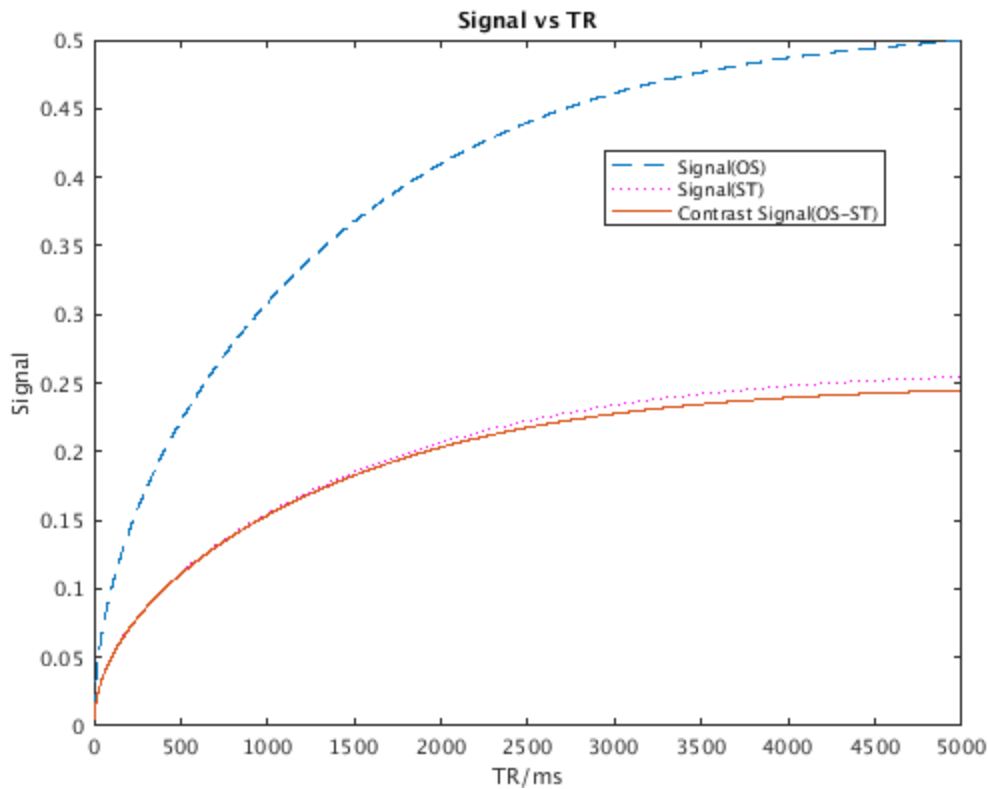
Figure 4.6: Graph of Signal against TR.

In Figure 4.6, we can see that the signals of OS and ST, as well as the signal contrast increase with increasing TR. This is because with longer TR, we are allowing more time for the spins to relax back to their equilibrium position, resulting in the longitudinal magnetisation approaching its maximum value before the application of the next RF pulse. When the next RF pulse is applied, the magnitude of the transverse magnetisation will be higher and so will be the signal detected. The signal intensities will stop increasing eventually after passing the point whereby all the spins have been fully relaxed.

However, having a long TR means that the acquisition time for the SWI scan will be long. This is not clinically favourable as the patients will have to lie still in the MRI scanner for long period of time which can cause great discomfort. Furthermore, having a long scan time can jeopardise the image quality due to unwanted background noise. Noise is a factor that we also aim to minimise from the image as it can cause difficulty in distinguishing ST from OS even when their contrast is very good. Due to these concerns, we turned our focus on improving the contrast-to-noise ratio (CNR) instead when doing the optimisation of TR.

With that, we carried out another simulation to observe how the CNR changes with TR. The results are shown in Figure 4.7.
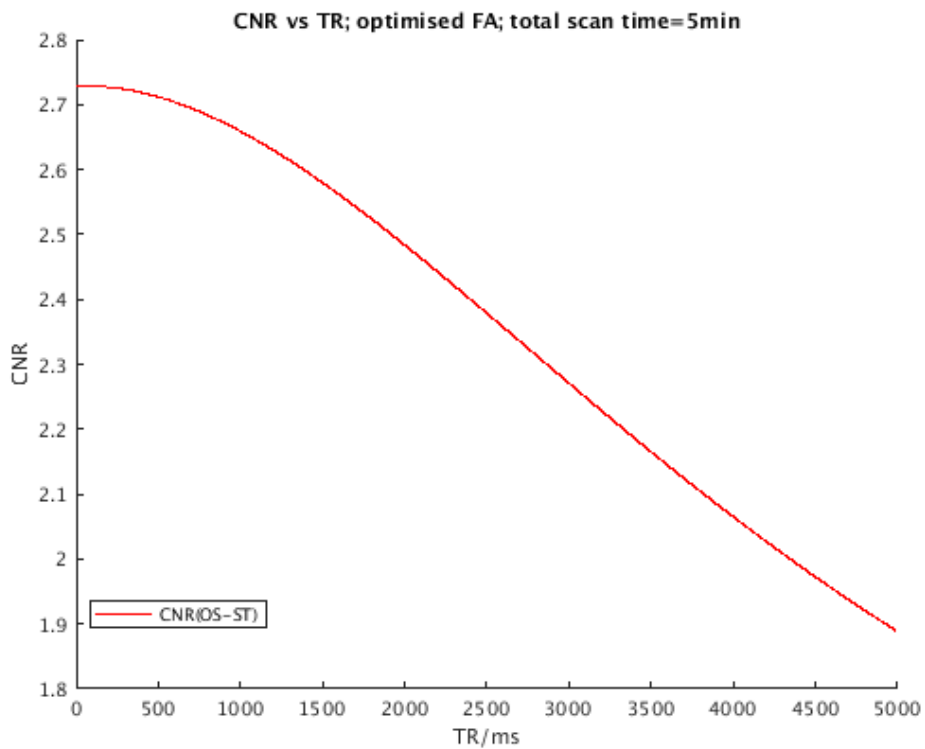
Figure 4.7: Graph of CNR against TR.

As expected, the CNR increases with decreasing TR as the number of acquisition increases. While it is debatable which TR we should choose to obtain the optimised image, we have decided to choose the shortest possible TR dictated by the MRI scanner. The short TR improves the CNR but may cause the contrast between ST and OS to suffer as seen in Figure 4.6. However, this should not be a concern as we have already optimised the contrast with the appropriate FA and TE. As such, the chosen TR will be around 60 ms.

5 Conclusions and Future Work

In this study, we have acquired MR images using the AFI, SPGR and GRE pulse sequences from healthy young volunteers at a field strength of 3T. From these data, we have successfully generated T_1 and T_2^* maps of the brain and measured the mean T_1 and T_2^* of our regions of interest, the swallow tail and the tissues surrounding the swallow tail.

The mean T_1 and T_2^* values of the swallow tail are 1358 ± 325 ms and 20.7 ± 4.9 ms respectively, and the mean T_1 and T_2^* values of the tissues surrounding the swallow tail are 1303 ± 337 ms and 41.3 ± 7.2 ms respectively.

After deriving the SWI equation which is found to be:

$$M_{xy} = \frac{M_0(1-\exp(-\frac{TR}{T_1}))\times\sin\alpha\times\exp(-\frac{TE}{T_2^*})}{1-\exp(-\frac{TR}{T_1})\times\cos\alpha},$$

we have completed the simulations to find the parameters that we should use to obtain the best contrasted SWI image of the swallow tail with maximum contrast-to-noise ratio. The optimised parameters are $\alpha_{optimal} = \cos^{-1}(\exp(-\frac{TR}{1255}))$, $TE_{optimal} = 27.8$ ms , and $TR_{optimal} \approx 60$ ms.

In conclusion, the objectives of this study have been fulfilled and we have successfully optimised the SWI sequence on Siemens 3T MAGNETOM Prisma. By using these optimised parameters, we will be able to obtain SWI images with a good contrast and resolution of the swallow tail sign in the substantia nigra from the healthy population. This will greatly increase the reliability and accuracy of the diagnosis of Parkinson's disease (PD) since a lack of swallow tail sign will very unlikely be caused by low signal contrast or poor resolution of the image. This is especially important as it enables patients to receive appropriate treatments to manage their symptoms.

Parkinson's disease is an age-related disease where the percentage of people developing it increases with age [20]. This is because ageing may affect the dopaminergic activities and other biological processes that lead to the degeneration of neurons of the brain. With that, further studies can be conducted on the healthy elderly population using the same methods as described in this report. We should find out whether the T_1 and T_2^* of the tissues are age dependent, and whether the optimised SWI parameters in the elderly population differ much from the younger

population. With a different set of optimised SWI parameters catered for a different age group, SWI will be more relevant in diagnosing PD for the wide range of population.

If possible, SWI with the optimised parameters can be conducted on healthy people and PD patients of the same age group. Group comparisons of the SWI images acquired from the healthy and PD population can be made to clearly visualise the difference in appearance of the substantia-nigra.

6 References

[1] CE4RT, Understanding Ionizing Radiation and Protection, CE4RT, 2014.

[2] S. Shams, D. Fallmar, S. Schwarz, L.-O. Wahlund, D. v. Westen, O. Hansson, E.-M. Larsson and X. S. Haller, "MRI of the Swallow Tail Sign: A Useful Marker in the Diagnosis of Lewy Body Dementia?," *American Journal of Neuroradiology,* vol. 38, no. 9, pp. 1737-1741, 2017.

[3] M. Gerlach, K. L. Double, M. B. H. Youdim and P. Riederer, "Potential sources of increased iron in the substantia nigra of parkinsonian patients," *Journal of Neural Transmission,* vol. 70, 2006.

[4] R. Sharma and A. Dixon, "Swallow tail sign (substantia nigra)," 2015. [Online]. Available: https://radiopaedia.org/articles/swallow-tail-sign-substantia-nigra.

[5] S. T. Schwarz, M. Afzal, P. S. Morgan, N. Bajaj, P. A. Gowland and D. P. Auer, "The 'Swallow Tail' Appearance of the Healthy Nigrosome – A New Accurate Test of Parkinson's Disease: A Case-Control and Retrospective Cross-Sectional MRI Study at 3T," *PLoS ONE,* vol. 9, no. 4, 2014.

[6] Z. R. Stephen, F. M. Kievit and M. Zhang, "Magnetite Nanoparticles for Medical MR Imaging," *Materials Today (Kidlington, England),* vol. 14, no. 7-8, pp. 330-338, 2011.

[7] R. W. Brown, Y.-C. N. Cheng, E. M. Haacke, M. R. Thompson and R. Venkatesan, Magnetic Resonance Imaging: Physical Principles and Sequence Design Second Edition, Hoboken, New Jersey: John Wiley & Sons, Inc, 2014.

[8] J. Ridgway, "Cardiovascular magnetic resonance physics for clinicians: Part I," *Journal of Cardiovascular Magnetic Resonance,* vol. 12, no. 1, 2010.

[9] A. Berger, "Magnetic resonance imaging," *BMJ,* vol. 324, no. 7328, p. 35, 2002.

[10] E. Haacke, S. Mittal, Z. Wu, J. Neelavalli and Y.-C. Cheng, "Susceptibility-Weighted Imaging: Technical Aspects and Clinical Applications, Part 1," *American Journal of Neuroradiology,* vol. 30, no. 1, pp. 19-30, 2009.

[11] S. Hidalgo-Tobon, "Theory of Gradient Coil Design Methods for Magnetic Resonance Imaging," *Concepts in Magnetic Resonance,* vol. 36, no. 4, pp. 223-242, 2010.

[12] F. Schweser, A. Deistung, B. Lehr and J. Reichenbach, "Differentiation between diamagnetic and paramagnetic cerebral lesions based on magnetic susceptibility mapping.," *Med Phys.,* vol. 37, no. 10, pp. 5165-5178, 2010.

[13] J. Wang, W. Mao, M. Qiu, M. B. Smith and R. T. Constable, "Factors influencing flip angle mapping in MRI: RF-pulse shape, slice-select gradients, off-resonance excitation, and Bo inhomogeneities," *Magnetic Resonance in Medicine 56,* vol. 56, no. 2, pp. 463-468, 2006.

[14] V. L. Yarnykh, "Actual Flip-Angle Imaging in the Pulsed Steady State: A Method for Rapid Three-Dimensional Mapping of the Transmitted Radiofrequency Field," *Magnetic Resonance in Medicine,* vol. 57, no. 1, pp. 192-200, 2007.

[15] S. C. Deoni, B. K. Rutt and T. M. Peters, "Rapid Combined T1 and T2 Mapping Using Gradient Recalled Acquisition in the Steady State," *Magnetic Resonance in Medicine,* vol. 49, no. 3, pp. 515-526, 2003.

[16] "MAGNETOM Prisma," 2018. [Online]. Available: https://www.healthcare.siemens.com/magnetic-resonance-imaging/3t-mri-scanner/magnetom-prisma.

[17] D. Mortimer, "FslView/UserGuide," 2016. [Online]. Available: https://fsl.fmrib.ox.ac.uk/fsl/fslwiki/FslView/UserGuide.

[18] R. George, J. D. Cruz, R. Singh and R. Ilangovan, "Signal-To-Noise Ratio and Image Quality," [Online]. Available: https://mrimaster.com/technique%20SNR.html.

[19] A. D. Elster, "Ernst Angle," 2017. [Online]. Available: http://mriquestions.com/optimal-flip-angle.html.

[20] J. V. Hindle, "Ageing, neurodegeneration and Parkinson's disease," *Age and Ageing,* vol. 39, no. 2, pp. 156-161, 2010.

[21] T. W. Redpath, "Calibration of the Aberdeen NMR imager for proton spin-lattice relaxation time measurements in vivo," *Physics in Medicine & Biology,* vol. 27, no. 8, pp. 1057-1065, 1982.